NASA/TM—2003-212253

# Bio-Optical and Geochemical Properties of the South Atlantic Subtropical Gyre

*S.R. Signorini*
*S.B. Hooker*
*C.R. McClain*

National Aeronautics and
Space Administration

**Goddard Space Flight Center**
Greenbelt, Maryland 20771

---

December 2003

The NASA STI Program Office … in Profile

Since its founding, NASA has been dedicated to the advancement of aeronautics and space science. The NASA Scientific and Technical Information (STI) Program Office plays a key part in helping NASA maintain this important role.

The NASA STI Program Office is operated by Langley Research Center, the lead center for NASA's scientific and technical information. The NASA STI Program Office provides access to the NASA STI Database, the largest collection of aeronautical and space science STI in the world. The Program Office is also NASA's institutional mechanism for disseminating the results of its research and development activities. These results are published by NASA in the NASA STI Report Series, which includes the following report types:

- TECHNICAL PUBLICATION. Reports of completed research or a major significant phase of research that present the results of NASA programs and include extensive data or theoretical analysis. Includes compilations of significant scientific and technical data and information deemed to be of continuing reference value. NASA's counterpart of peer-reviewed formal professional papers but has less stringent limitations on manuscript length and extent of graphic presentations.
- TECHNICAL MEMORANDUM. Scientific and technical findings that are preliminary or of specialized interest, e.g., quick release reports, working papers, and bibliographies that contain minimal annotation. Does not contain extensive analysis.
- CONTRACTOR REPORT. Scientific and technical findings by NASA-sponsored contractors and grantees.
- CONFERENCE PUBLICATION. Collected papers from scientific and technical conferences, symposia, seminars, or other meetings sponsored or cosponsored by NASA.
- SPECIAL PUBLICATION. Scientific, technical, or historical information from NASA programs, projects, and mission, often concerned with subjects having substantial public interest.
- TECHNICAL TRANSLATION. English-language translations of foreign scientific and technical material pertinent to NASA's mission.

Specialized services that complement the STI Program Office's diverse offerings include creating custom thesauri, building customized databases, organizing and publishing research results . . . even providing videos.

For more information about the NASA STI Program Office, see the following:

- Access the NASA STI Program Home Page at http://www.sti.nasa.gov/STI-homepage.html
- E-mail your question via the Internet to help@sti.nasa.gov
- Fax your question to the NASA Access Help Desk at (301) 621-0134
- Telephone the NASA Access Help Desk at (301) 621-0390
- Write to:
  NASA Access Help Desk
  NASA Center for AeroSpace Information
  7121 Standard Drive
  Hanover, MD 21076–1320

NASA/TM—2003–212253

# Bio-Optical and Geochemical Properties of the South Atlantic Subtropical Gyre

*S.R. Signorini, Stanford B. Hooker, Charles R. McClain,*
*Goddard Space Flight Center, Greenbelt, MD*

National Aeronautics and
Space Administration

**Goddard Space Flight Center**
Greenbelt, Maryland 20771

December 2003

Available from:

NASA Center for AeroSpace Information
7121 Standard Drive
Hanover, MD 21076–1320
Price Code: A17

National Technical Information Service
5285 Port Royal Road
Springfield, VA 22161
Price Code: A10

## 1. Introduction

An investigation of the bio-optical properties of the South Atlantic subtropical gyre (SASG) was conducted using data primarily from the UK Atlantic Meridional Transect (AMT) program and SeaWiFS. The AMT cruises extend from the UK to the Falklands Islands (sailing on the RRS *James Clark Ross*) with the purpose of improving our knowledge of surface layer hydrography, biogeochemical processes, ecosystem dynamics and food webs across basin scales in the Atlantic Ocean [*Aiken et al.*, 2000]. Two objectives of the AMT program relevant to this study are the characterization of biogeochemical provinces and the analysis of optical and pigment parameters in connection with remote sensing ocean color data.

The primary focus of this NASA Technical Memorandum is on the variability of the vertical distribution of phytoplankton pigments and associated absorption properties across the SASG, and their relevance to remote sensing algorithms. Therefore, a subset of the AMT data within the SASG from all available cruises was used in the analyses. One of the challenges addressed here is the determination of the SASG geographic boundaries. One of the major problems is to reconcile the properties of biogeochemical provinces [*Longhurst et al.*, 1995] with the boundaries of physical provinces [*Hooker et al.*, 2000b]. We use water mass analysis, dynamics of ocean currents, and meridional gradients of bio-optical properties, to identify the SASG boundaries.

The variability of the sea-air $pCO_2$ difference ($\Delta pCO_2$) and corresponding $CO_2$ flux are also analyzed in this TM. Atmospheric and oceanic $pCO_2$ were measured continuously [*Lefevre and Moore*, 2000] along an AMT transect ($50^oN$-$50^oS$) in September-October 1995 and 1996 (UK to the Falklands Islands) and in April-May 1996 (Falklands Islands to the UK). Based on data from these three AMT cruises, and data from two other cruises (M/V *Prince of Seas* sailing from UK to Jamaica and RMS *St. Helena* sailing from UK to South Africa), *Lefevre and Taylor* [2002] developed a $pCO_2$ algorithm for the North Atlantic and South Atlantic gyres. We used the $pCO_2$ algorithm to estimate the seasonal variability of $\Delta pCO_2$ and sea-air $CO_2$ flux in the SASG.

## 2. Data Sources and Methods

A variety of data sources were used in this study. However, the major sources were the AMT cruises and SeaWiFS data. The AMT cruises (Table 1) provided the bulk of the *in situ* data analyzed. These included CTD and XBT data, nutrients, pigments, and apparent optical properties (AOP) of seawater covering the majority of the SeaWiFS channels. The only pigment analyzed in this study is the total chlorophyll *a*, defined as TChl *a* = [chlorophyllide *a* + divinyl chlorophyll *a* + chlorophyll *a*]. Other ancillary data sets were used to complement the analyses. Climatological temperature and salinity data from the World Ocean Atlas 98 (WOA98) [*Conkright et al.*, 1998] were used to derive dynamic height and geostrophic currents. WOA98 salinity data were used for calculating $CO_2$ solubility and weekly SST global fields [*Reynolds and Smith*, 1994] were used in conjunction with the $pCO_2$ algorithm. Long records of atmospheric $CO_2$ (Atm_$pCO_2$) are not available for the South Atlantic. Therefore, monthly 10-year records (July 1991 – December 2001) of atmospheric $pCO_2$ concentrations from the CSIRO GASLAB flask sampling network in the South Pacific, were used to produce weekly Atm_*p*CO$_2$ interpolated in latitude at 1$^o$ resolution to conform with the SST grid. The secular trend of atmospheric CO$_2$ does not change significantly throughout the Earth's atmosphere, but the seasonal cycle does. However, meridional gradients of atmospheric CO$_2$ over the ocean are much larger than zonal gradients due to the dynamics of the atmospheric circulation [*Craig et al.*, 1998]. Therefore, the zonal extrapolation of the atmospheric CO$_2$ records from the South Pacific to the South Atlantic is appropriate. Data from three Australian stations were used: Cape Ferguson (19$^o$17'S, 147$^o$03'E), Cape Grim (40$^o$41'S, 144$^o$41'E), and Macquarie Island (54$^o$29'S, 158$^o$58'E). These data were downloaded from the Carbon Dioxide Information Analysis Center (CDIAC) web site (cdiac.esd.ornl.gov).

Five-day global SSM/I winds (July 1991–December 2002) were used to derive gas transfer coefficient values for the calculation of sea-air CO$_2$ flux. Monthly climatological winds from the NCEP/NCAR Reanalysis Project were used to calculate Ekman pumping and Ekman drift.

**Table 1.** Summary of parameters observed (Station=ST and Underway=Undwy) on AMT cruises. Not all parameters were analyzed in this study.

| **Cruise** | **Dates (0$^o$ to 40$^o$S)** | **Observed Parameters** |
|---|---|---|
| AMT-1 | Oct 8-22,1995 | T,S (CTD and Undwy), T (XBT), ST Nutrients, Pigments (ST&Undwy), PAR, Reflectances |
| AMT-2 | May 9-20, 1996 | T,S (CTD and Undwy), T (XBT), ST Nutrients, Pigments (ST&Undwy), PAR, Reflectances |
| AMT-3 | Oct 6-23, 1996 | T,S (CTD and Undwy), T (XBT), ST Nutrients, Pigments (ST&Undwy), PAR, Reflectances |
| AMT-4 | April 23-May10, 1997 | T,S (CTD and Undwy), T (XBT), ST Nutrients, Pigments (ST&Undwy), PAR, Reflectances |
| AMT-5 | Oct 3-14, 1997 | T,S (CTD and Undwy), T (XBT), ST Nutrients, Pigments (ST&Undwy), PAR, Reflectances |
| AMT-6B | April 4-18, 1998 | T,S (CTD and Undwy), T (XBT), Pigments (ST&Undwy), PAR, Reflectances |
| AMT-6 | May 15-31, 1998 | T,S (CTD and Undwy), T (XBT), Pigments (ST&Undwy), PAR, Reflectances |
| AMT-7 | Oct 5-22, 1998 | T,S (CTD and Undwy), T (XBT), Pigments (ST&Undwy), PAR, Reflectances |
| AMT-8 | April 27 - May 20, 1999 | T,S (CTD and Undwy), T (XBT), Pigments (ST&Undwy), PAR, Reflectances |
| AMT-9 | Oct 2-12, 1999 | T,S (CTD and Undwy), T (XBT) |

## *2.1 Hydrography*

The circulation and frontal zones of the South Atlantic Ocean, with the locations of the AMT stations superposed, are shown in Figure 1. The station locations for the repeat cruises (AMT 1, 2, 3, 4, 5, 6B, 7, and 9) are shown parallel to the coast of South America. These cruises were conducted during the austral fall (even numbers) and spring (odd numbers). Two other cruises were conducted only once during austral fall. Cruise

AMT-6 went through the Angola Dome and the Benguela coastal upwelling system, while cruise AMT-8 traversed the SASG far offshore. This study focuses on the westernmost repeat cruises off the coast of South America, and it is limited to the latitude range between the equator and 40°S, e.g., the subtropical gyre and its poleward and equatorward circulation boundaries. The analyses of the hydrographic and bio-optical data collected during these cruises will be discussed in the forthcoming sections.

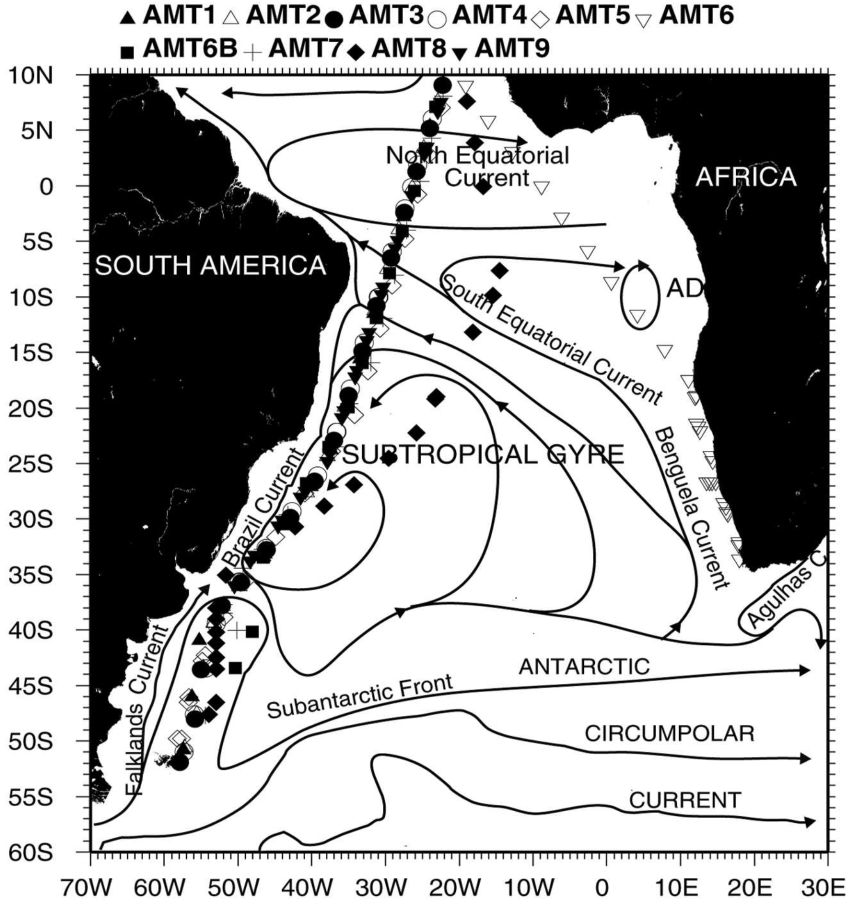

**Figure 1.** The current system and frontal zones of the South Atlantic Ocean (adapted from Peterson and Stramma, 1991). The location of the AMT stations (AMT-1, 2, 3, 4, 5, 6, 6B, 7, 8, and 9) are superposed. This study focuses on the westernmost AMT stations off the coast of South America, and is limited to the latitude range of $0^o$ - $40^o$S.

The CTD stations were conducted every 500km on average and the maximum sampling depth, within the latitude range analyzed here ($0^o$ – $40^o$S), never exceeded 200m. The XBT data have much higher meridional resolution and deeper sampling depths. The average distance between XBT drops is 95km with a maximum sampling depth of 760m. The vertical resolution of both XBT and CTD data is ~1m.

A net change criterion [*Sprintall and Cronin*, 2001] is used to derive the mixed layer depth (MLD) as the depth at which:

$$\rho(z=\mathrm{MLD})=\rho(z=0)-\Delta T\frac{\mathrm{d}\rho}{\mathrm{d}T} \tag{1}$$

where $\rho(z=0)$ is the surface density (kg m$^{-3}$), $\Delta T$ is the net change in temperature from the surface (0.5°C), and $\mathrm{d}\rho/\mathrm{d}T$ is the thermal expansion coefficient (kg m$^{-3}$ °C$^{-1}$) calculated from the equation of state of sea water using surface temperature and salinity values.

### *2.2 Optical Data Collection Methods, Calibration, and Derived Parameters*

The calibration and validation of remotely sensed observations of ocean color is an inherent objective of AMT cruises: first, by relating *in situ* observations of water-leaving radiances, $L_W(\lambda)$, to satellite measurements, and second, by measuring the bio-optically active constituents of the water. The former was the reason for the emphasis on measuring the apparent optical properties (AOPs) of seawater. The optical instruments used were a mixture of traditional winch and crane designs and free-fall systems. The advantage of the latter is they can be deployed far enough away that the light observations are not contaminated by the presence of the ship.

All of the profiling instruments measured the upwelling radiance and downward irradiance, $L_u(\lambda)$ and $E_d(\lambda)$, respectively. Some of the systems also measured the upward irradiance, $E_u(\lambda)$, and the global solar irradiance, $E_d(0^+,\lambda)$, was always recorded when in-water data were acquired. The evolution in the optical instruments and the validation of their new capabilities is documented by *Robins et al.* [1996], *Aiken et al.* [1998], and *Hooker and Lazin* [2000]. The spectral band set varied with some instruments, but all sensors had a standard set of seven wavelengths that covered the majority of the SeaWiFS channels: 412, 443, 490, 510, 555, 665, and 683 nm.

To ensure that the quality of the data were as accurate as possible, a concerted effort was made to investigate the total uncertainty budget for a continuing series of established, new, and refined instrument designs. A comprehensive approach was undertaken that included the following:

- The use of a portable light source, the SeaWiFS Quality Monitor (SQM), to monitor the calibration stability of the instruments in the field [*Hooker and Aiken*, 1998; *Johnson et al.*, 1998];
- Investigation of the uncertainties in the data processing scheme [*Hooker et al.*, 2001]; and
- Intercalibration round robins to assess the uncertainties in the calibration process [*Hooker et al.*, 2002].

These inquiries not only concentrated on the diversity of in-water instruments, but also on alternative methods for acquiring solar reference data. They also involved the estimation of important ancillary measurements, like the uncertainties associated with the determination of pigment concentrations using HPLC techniques [*Claustre et al.*, 2003; *Hooker et al.*, 2000a].

The culmination of this extensive investigation of uncertainties was a confirmation that the field measurements usually satisfy the SeaWiFS accuracy requirements for calibration and validation activities [*Hooker and Maritorena*, 2000; *Hooker et al.*, 2003]. Although this result is primarily applicable to the water-leaving radiances and their immediate by-products (e.g, the remote sensing reflectances or the normalized water-leaving radiances), most of the other potentially useful bio-optical parameters are derived directly from the same basic measurement parameters:

- The photosynthetically available radiation (PAR) at the surface, $E_{\mathrm{PAR}}(0^+)$, the in-water decay of which is used primarily to determine the depth of the 1% light level (the so-called *euphotic* depth, $Z_e$);
- The diffuse attenuation of seawater determined from the upwelled radiance ($K_{Lu}$) or the downward irradiance ($K_d$);
- The mixed layer depth (MLD) and the value of PAR at the MLD, the so-called *penetration irradiance*, $E_{\mathrm{PAR}}(Z_e)$;
- The depth of the chlorophyll maximum (DCM); and
- The chlorophyll *a* concentration ([TChl *a*]) determined by HPLC analysis and by inverting the optical measurements with the OC4v4 algorithm.

## 3. South Atlantic Circulation and Subtropical Gyre Domain

The dominant feature of the South Atlantic circulation, as in other mid-latitude ocean basins, is the anticyclonic flow around the subtropical gyre (see Figure 1 for main South Atlantic circulation features). However, a unique feature of the gyre-scale flow in the South Atlantic is the strong influence of interocean connections [*Reid*, 1989]. At the southern tip of South America, the South Atlantic Subtropical Gyre (SASG) acquires cold sub-Antarctic mode water and Antarctic intermediate water from the Pacific Ocean inflow within Drake Passage [*Witter and Gordon*, 1999]. Further north, strong frontal features and energetic eddies are formed at the Brazil-Malvinas Confluence resulting from the merging of sharply contrasting circumpolar and South Atlantic thermocline waters [*Peterson and Stramma*, 1991]. At the southernmost coast of Africa, eddies shed from the Agulhas Current Retroflection (ACR) and drift westward across the South Atlantic near 30$^{\circ}$S carrying Indian Ocean water [*Gordon et al.*, 1992; *Witter and Gordon*, 1999]. These eddies feed blended water masses via the Benguela Current into the SASG [*Gordon*, 2003]. The Benguela Current turns seaward as the South Equatorial Current (SEC), which bifurcates at the South American coast near 10$^{\circ}$S (Figure 1) in the surface layer and near 25$^{\circ}$S at Antarctic intermediate water depths [*Witter and Gordon*, 1999]. The northward flowing branch within the North Brazil Coastal Current (NBCC) crosses into the Northern Hemisphere, providing a conduit for exchange between the South and North Atlantic Oceans. The circulation along the coastal regions of western Africa also interacts with the SASG. Off the Angola coast, between 10$^{\circ}$S and 15$^{\circ}$S, there is a cyclonic gyre that maintains the Angola Dome, a dome-like subsurface distribution of hydrographic properties dynamically balanced by the cyclonic flow. Strong wind divergence along the coast drives the Benguela coastal upwelling system (top plate in Figure 1).

The seasonal circulation in the South Atlantic is represented in Figure 2, which shows the seasonal dynamic height and corresponding geostrophic currents derived from the World Ocean Atlas 1998 [*Conkright et al.*, 1998] hydrographic data. The dynamic height is integrated from 2000m to the surface. No current vectors are plotted between 0$^{\circ}$ and 5$^{\circ}$S because the geostrophic balance breaks down near the equator where the Coriolis

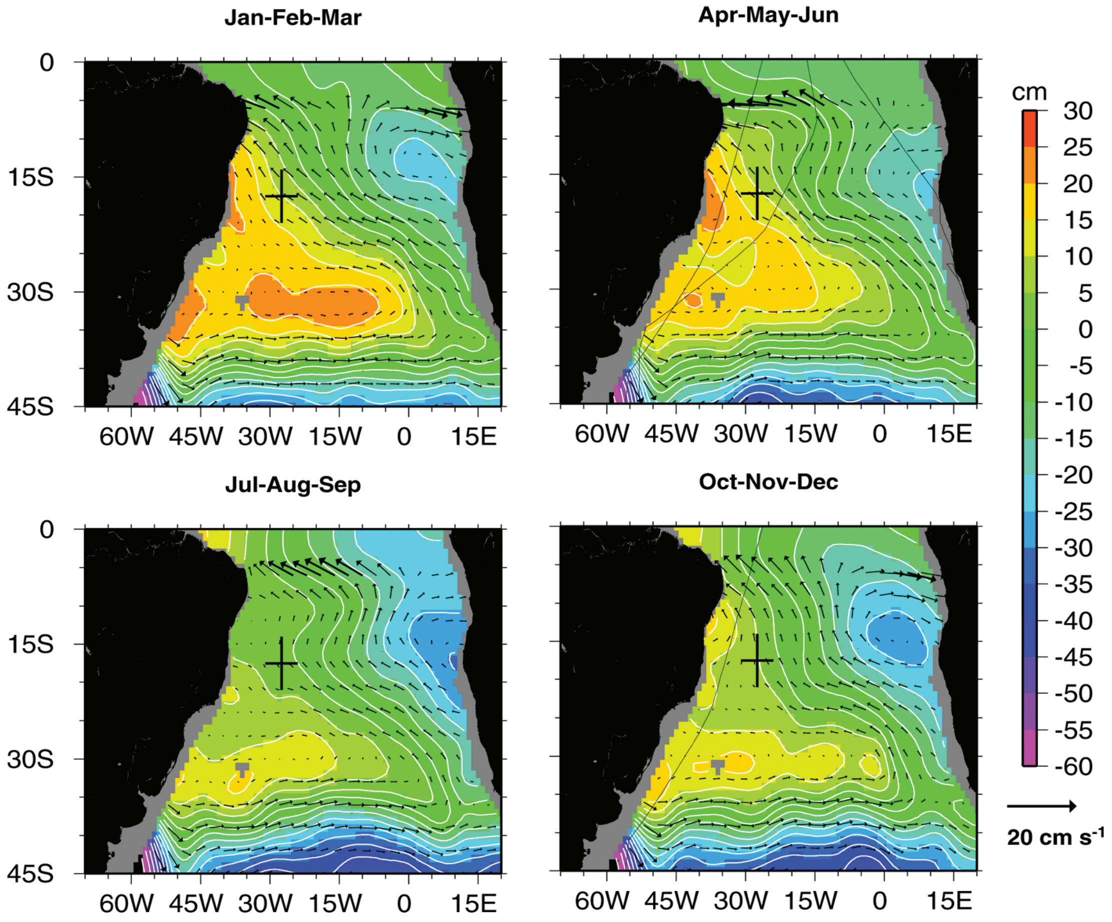

**Figure 2**. Seasonal dynamic height and geostrophic currents in the South Atlantic based on World Ocean Atlas 1998 hydrography. The dynamic height reference level is 2000 m. The cross shows the location and standard deviation of the climatological chlorophyll minimum location obtained from SeaWiFS data. The black lines are the AMT cruise tracks.

parameter vanishes. Also, the narrow western boundary currents, i.e., the Brazil and Malvinas currents, are not represented in Figure 2 due to the coarse resolution (1$^{o}$) of the temperature and salinity gridded fields. Two distinct gyres are present in all seasons, the anticyclonic SASG and the Angola Dome cyclonic gyre (ADG). The strength and size of these gyres vary from season to season. The SASG is larger and swifter during April-June and smaller and weaker during October-December. As the SASG expands, the ADG contracts, and vice-versa. The dynamic center of the region of maximum dynamic height is centered near 30$^{o}$S and 35$^{o}$W-45$^{o}$W during most seasons. The cross in Figure 2 shows the location and standard deviation of the climatological (September 97 – August 02) chlorophyll minimum obtained from SeaWiFS data [*McClain et al.*, 2003]. The location of the chlorophyll minimum seems incoherent with the circulation as it lies in a region of relatively strong currents (compared to currents further to the SE) and the dynamic center of the gyre where the pycnocline (nutricline) is deepest. However, the chlorophyll concentration should be more coherent with the shallow circulation within the mixed layer (10-120m) and euphotic zone (~100m) depths rather than the much deeper currents. A different rendition of the dynamic height and geostrophic currents, using 500m as the level of reference, is provided in Figure 3. This level of reference was also used by *Signorini* [1978] to compute the volume transport of the Brazil Current near 23$^o$S at ~10 Sv, in agreement with values obtained from more recent studies [*Evans and Signorini*, 1985; *Evans et al.*, 1983; *Stramma*, 1989].

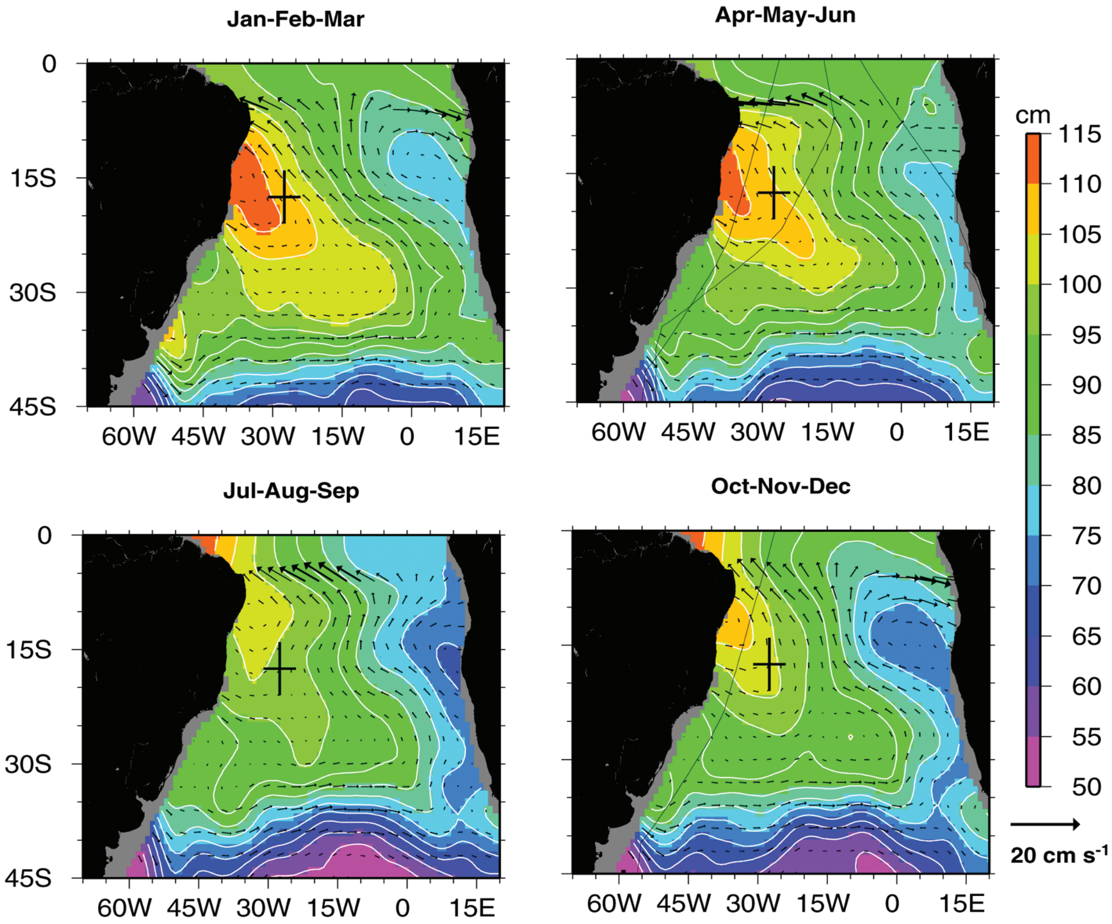

**Figure 3.** Seasonal dynamic height and geostrophic currents in the South Atlantic based on World Ocean Atlas 1998 hydrography. The dynamic height reference level is 500 m. The cross shows the location and standard deviation of the climatological location of the chlorophyll minimum obtained from SeaWiFS data. The black lines are the AMT cruise tracks.

This shallower rendition of the geostrophic circulation seems more coherent with the chlorophyll minimum location, which is now much closer to the maximum dynamic height. The 0/500m dynamic height distribution is very similar to the seasonal depth of the 25.5 $\sigma_t$ surface and the depth of the 2 $\mu$M nitrate concentration (not shown). This $\sigma_t$ surface is chosen to be a proxy for the pycnocline depth and ranges seasonally from 160 to 180m. The relatively small misalignment between the maximum dynamic height (Figure 3) and the chlorophyll minimum location may be a result of spatially and temporally sparse hydrographic data available to produce the seasonal climatology, as well as the different time periods for averaging the SeaWiFS and hydrographic data sets. The coarseness of the hydrographic data is evident by the absence of the narrow and swift Brazil Current on the western boundary. The seasonal contraction/expansion of the SASG and ADG is also evident in Figure 3.

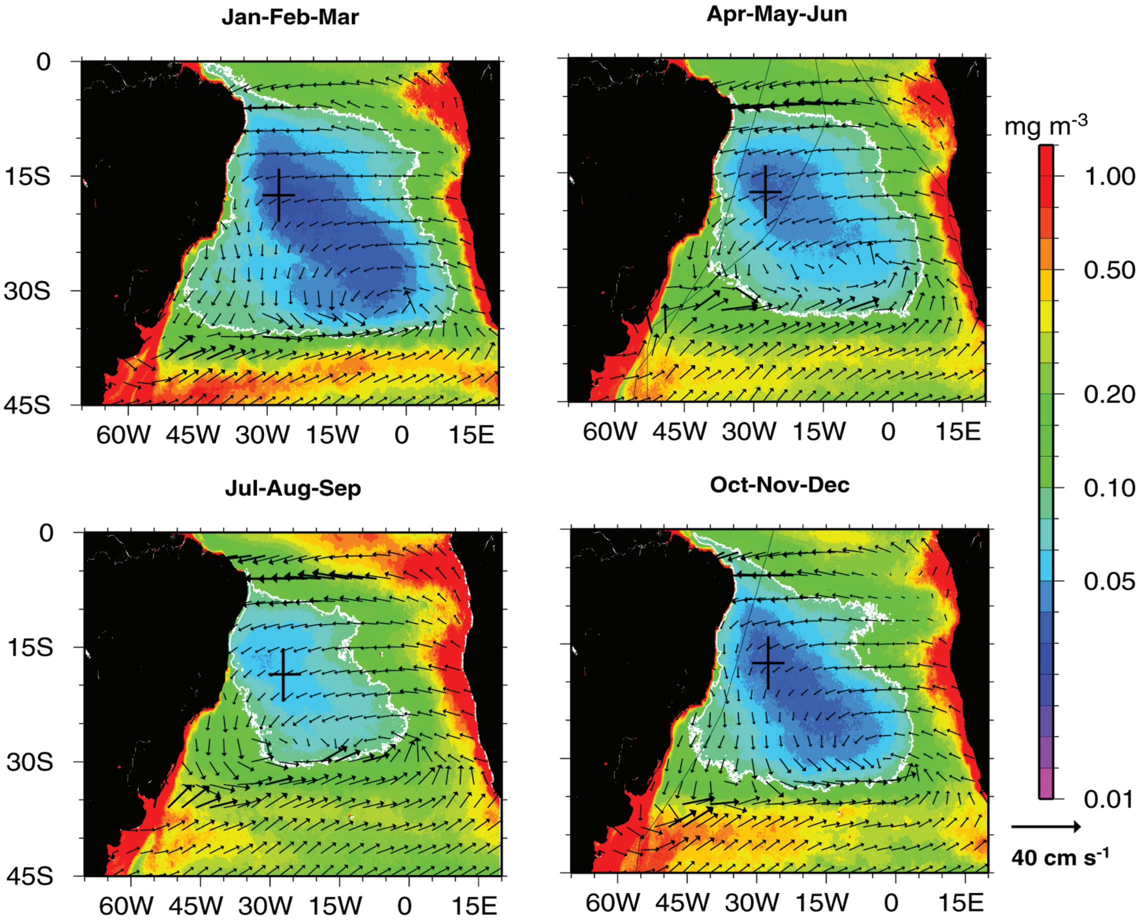

**Figure 4.** SeaWiFS seasonal chlorophyll climatology for the South Atlantic, with seasonal surface currents (geostrophic plus Ekman drift) superimposed. The white lines are the 0.1mg $m^{-3}$ TChl *a* contours. The cross shows the location and standard deviation of the minimum climatological chlorophyll obtained from SeaWiFS data. The black lines are the AMT cruise tracks.

The seasonal chlorophyll climatology derived from SeaWiFS data is shown in Figure 4. The seasonal surface currents (geostrophic with reference at 500m plus Ekman drift) are superposed. The contours of the 0.1mg $m^{-3}$ TChl *a* concentration (white lines) are also plotted. The surface currents and the TChl *a* spatial distribution are very coherent. Areas that are expected to be nutrient rich have TChl *a* concentrations greater than 0.5mg $m^{-3}$. Along the west coast of Africa, offshore-directed currents transport nutrients and phytoplankton from the Benguela coastal upwelling region and Congo River mouth towards the interior of the gyre. Northeastward surface currents along the Subtropical Front (STF) near 40°S carry nutrient-rich waters from the Southern Ocean northward into the gyre. As the currents intensify towards the gyre interior (Figure 4, July-September) more nutrients are entrained into the gyre and the size of the oligotrophic region contracts [*McClain et al.*, 2003].

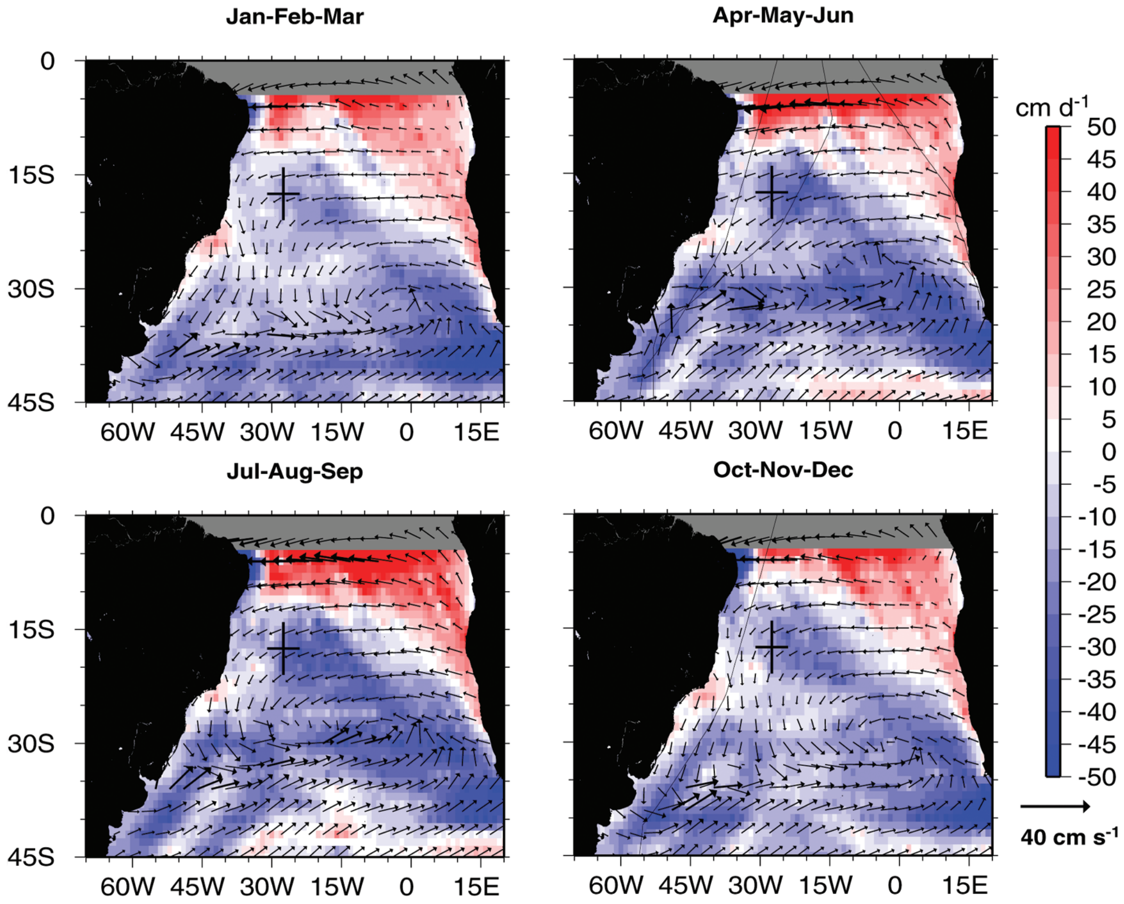

**Figure 5.** Seasonal climatology of Ekman pumping for the South Atlantic with seasonal surface currents (geostrophic + Ekman drift) superimposed. The cross shows the location and standard deviation of the minimum climatological chlorophyll obtained from SeaWiFS data. The black lines are the AMT cruise tracks.

This mechanism of nutrient supply has been demonstrated for the North Atlantic subtropical gyre [*Oschlies*, 2002a; *Oschlies*, 2002b; *Williams and Follows*, 1998] and can be extended to the other gyres. The Ekman transport is directed towards the gyre centers in all anticyclonic large-scale circulation systems, and the fringes of the subtropical gyres interact with nutrient-rich water masses.

The seasonal Ekman pumping is shown in Figure 5 with the surface currents (geostrophic + Ekman drift) superposed. The interior of the gyre is dominated by downwelling, while in the regions of the ADG, the SEC, and Benguela Current, strong upwelling is present in all seasons. There is stronger downwelling extending from the region of the chlorophyll minimum to the southeast region of the SASG where the curl of the wind has its largest negative value in all seasons. Despite the strong downwelling in the gyre's interior, chlorophyll concentrations can be as high as 0.2-0.4 mg $m^{-3}$ inside the gyre (see Figure 4 for Jul-Aug-Sep). As previously mentioned, an important mechanism for the transport of nutrients from the gyre fringes to its interior is the surface circulation (geostrophic currents + Ekman transport).

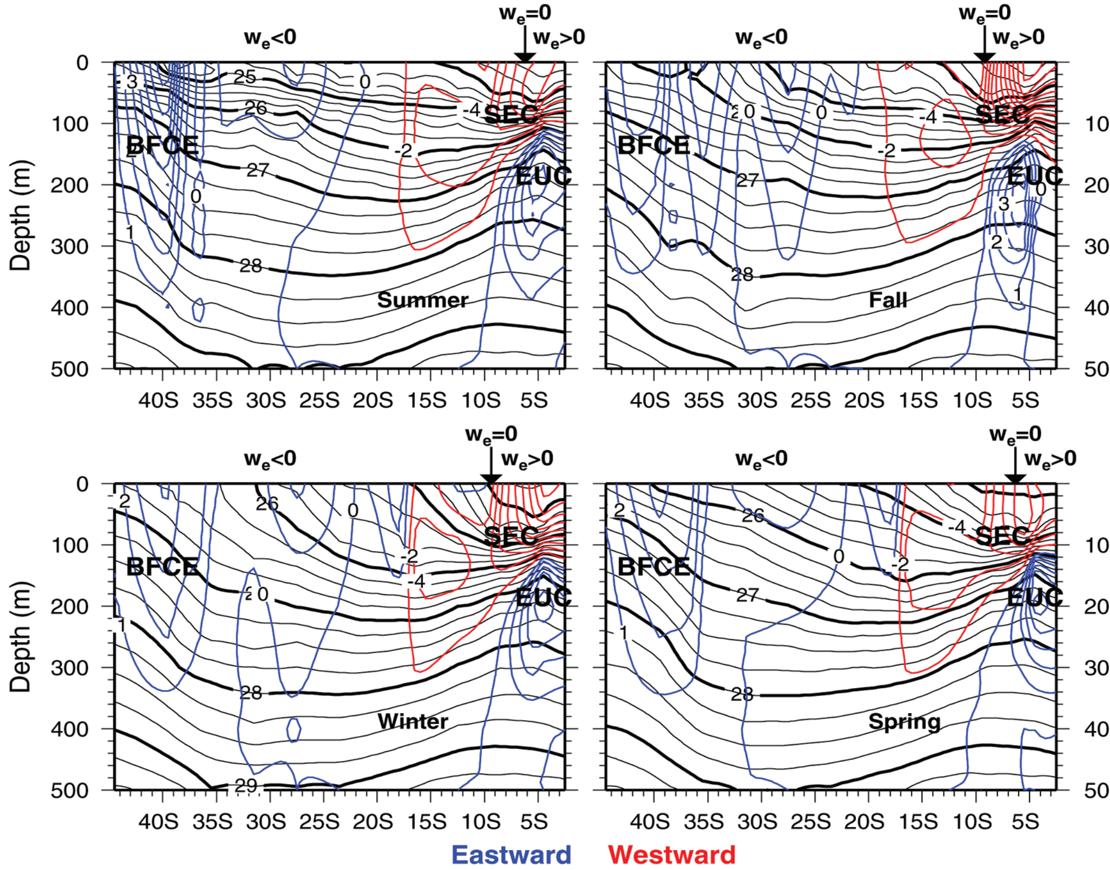

**Figure 6.** Seasonal transects of $\sigma_t$ (black contours) and cross-transect geostrophic velocity (blue eastward, red westward). The reference level is 500m. The regions of Ekman downwelling ($w_e < 0$) and upwelling ($w_e > 0$) are separated by the downward vector on top of each transect. The $\sigma_t$ and geostrophic velocity are derived from WOA98 [*Conkright et al.*, 1998] temperature and salinity climatology at one-degree points along the AMT cruise track. The major currents are labeled SEC (South Equatorial Current), EUC (Equatorial Under Current), and BFCE (Brazil-Falkland Confluence Extension, or South Atlantic Current).

The SASG is bound to the north by the southern branch of the SEC, to the south by the South Atlantic Current (SAC), to the west by the Brazil Current (BC), and to the east by the Benguela Current. These oceanic currents are characterized by fronts identified by strong horizontal density (dynamic height) gradients (see Figures 2 and 3), which are regions of intense aggregation of biological activity. Therefore, it is expected to find intensified gradients of biomass along oceanographic fronts. Seasonal transects of $\sigma_t$, and cross-transect geostrophic velocity (cm $s^{-1}$), are shown in Figure 6. The $\sigma_t$ and geostrophic velocity (with reference to 500 m) were derived from WOA98 temperature and salinity seasonal climatology [*Conkright et al.*, 1998], at one-degree grid points along the AMT cruise track. The regions of Ekman upwelling/downwelling ($\pm w_e$) are shown at the top of each seasonal transect, with the region of zero wind stress curl ($w_e$=0) indicated by the vertical arrow, which changes seasonally between 7°S and 10°S. The westward SEC is clearly shown between the equator and 15°S, above the eastward Equatorial Undercurrent (EUC). The SAC, labeled as the Brazil-Falkland Confluence Extension (BFCE), is centered near 40°S. The SASG lies between the equatorial and subtropical front current regimes, in a region characterized by Ekman downwelling in all seasons.

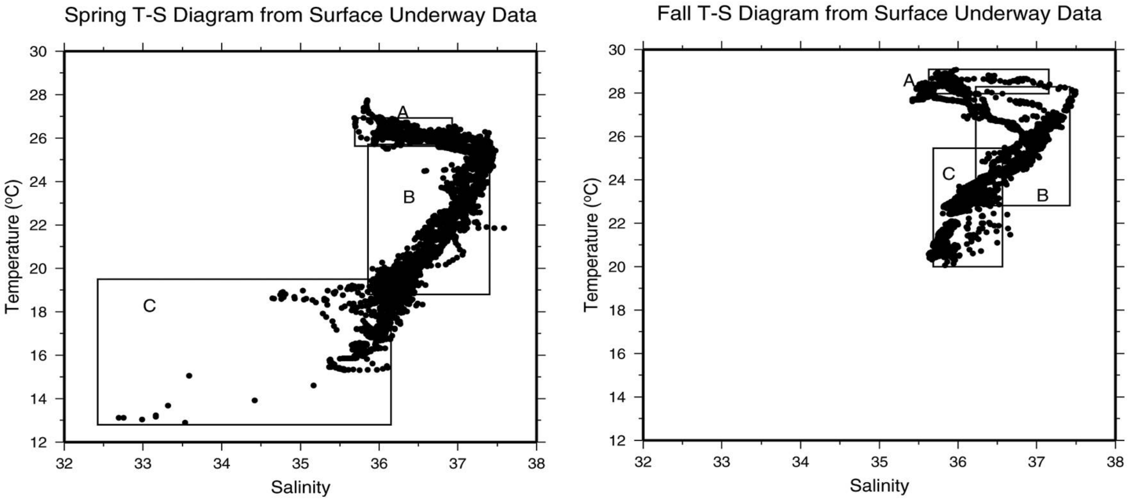

**Figure 7.** Spring and fall T-S diagrams from surface underway temperature and salinity observations. Three water masses are identified following Hooker et al. (2000): A) the South Equatorial Current (1°N - 15°S); B) the South Atlantic Subtropical Gyre (15°S - 30°S); and, C) the Brazil Current (BC). In the spring, some of the BC water mass is diluted with fresher coastal water influenced by the La Plata River discharge.

These current systems are associated with very distinct water masses. For the purposes of this study, which has its main focus on remote sensing applications, the water mass analysis that follows concentrates on the surface layer only. The temperature-salinity diagrams (T-S) for spring (AMT-1, 3, 5, 6B, 7, and 9) and fall (AMT-2, 4, and 8) cruises, obtained from underway near-surface T-S observations, are shown in Figure 7. The boxes labeled A, B, and C delimit the temperature and salinity ranges [*Hooker et al.*, 2000b] of the SEC, SASG, and Brazil Current, respectively. The latitudinal extent of the SEC, SASG, and BC water mass signatures along the AMT cruise track are, respectively, 1°N–15°S, 15°S–30°S, 30°S–35°S, but the surface T-S characteristics of the SEC and SASG extend much farther offshore [*Hooker et al.*, 2000b]. The knee on the T-S diagram, identified by a sharp decrease in salinity with relatively small change in temperature, separates the SEC waters from the saltier and colder SASG waters. There is a very tight T-S relationship for these waters, contrasting with the more scattered T-S relationship within box C, especially during spring. The water mass bounded by box C is a mixture of tropical water from the Brazil Current and fresher and colder coastal waters. During spring, the coastal waters are much colder and fresher, a result of elevated freshwater discharge from the La Plata River, which affected the nearshore AMT stations at 35°S. The separation between the SEC and SASG water masses on the fall T-S diagram is not as sharp as for spring. This is mainly due to the inclusion of AMT-8 data, which crossed the equator much farther east than the other even-numbered cruises, thus sampling a much stronger upwelling regime.

The circulation and water mass distribution influence the biology of the SASG region. Figure 8 shows meridional chl *a* gradients derived from along-track SeaWiFS seasonal climatology. The gradients are very small in the gyre's interior, while there are abrupt changes at the gyre fringes shown by large jumps in the meridional gradients. The meridional variability of the chlorophyll gradients is consistent with the location of the fronts obtained from the analyses of T-S properties and geostrophic currents.

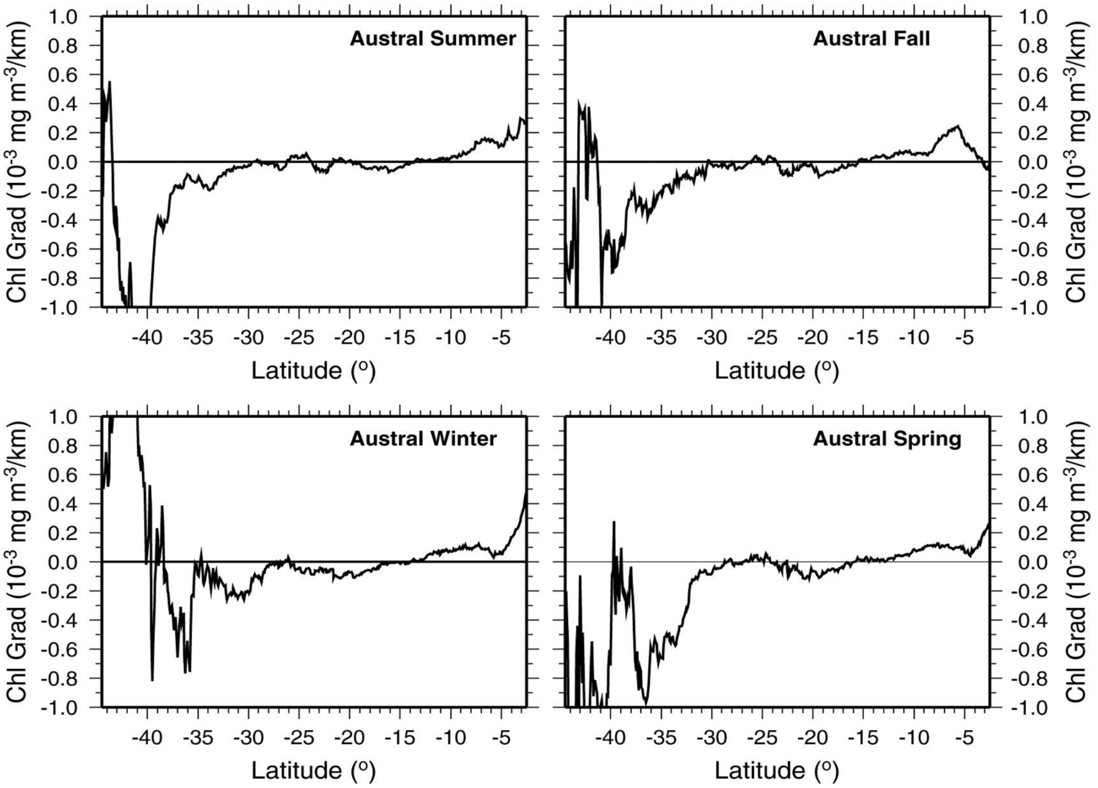

**Figure 8**. Seasonal variability of meridional chlorophyll gradients from along-track SeaWiFS climatology.

## 4. Upper Ocean Properties

This section addresses the meridional variability of the upper ocean physical properties and nutrient distribution based on the hydrographic (XBT, CTD, and nutrients) and subsurface irradiance data from the AMT cruises. The data are shown as individual transects ($\sigma_t$ and subsurface irradiance) and sorted and combined to produce transects for the two sampled seasons, Austral spring (odd numbered cruises) and fall (even numbered cruises). The AMT cruises were limited to investigating only the spring and fall seasons in the Atlantic because of the logistic program of the research vessel. Only the portion of the cruise tracks covering the SASG and its poleward and equatorward boundaries ($0^{o}$–$40^{o}$S) are analyzed. Detailed descriptions of the AMT program, synthesis of data, and identification of oceanic provinces ($50^{o}$N–$50^{o}$S) are provided elsewhere [*Aiken and Bale*, 2000; *Aiken et al.*, 2000; *Hooker et al.*, 2000b] and will not be reproduced here.

### *4.1 Upper Ocean Vertical Structure*

Figure 9 shows meridional transects of CTD-derived $\sigma_t$ for spring (AMT1,3,5,7,9) and fall (AMT2,4,6B). The $\sigma_t = 25.5$ isopycnal, which is defined as the pycnocline depth, is shown as a thick white line in all transects. The mixed layer depth is shown in all transects by the thin white line. The black vertical thin lines indicate the CTD casts.

Note that the mean dates for the spring cruises (AMT-1, 3, 5, 6, and 9) are within a few days apart in October of each year, while the mean dates for the fall cruises (AMT-2, 4, 6B) differ by two weeks to one month (May 15, 1996; May 1, 1997; and April 11, 1998, respectively). The differences in sampling time seem to be one of the reasons why the density gradients between AMT-2 and AMT-4 within 32.5°S–40°S, and between AMT-6B and AMT-2,-4 within 10°S and the equator, differ so much. Therefore, some of the interannual variability deduced from these transects are an artifact of sampling different seasonal stages of the natural variability.

North of 20°S the MLD is always shallower than the pycnocline in spring and fall. The pycnocline is deepest (140–180m) near the center of the gyre (15°S–20°S). In the spring the pycnocline is ventilated to the surface within 25°S–40°S, with some noticeable interannual changes. The ventilation zone reached its farthest northward influence (22°S) in the spring of 1999 (AMT9), while in the spring of 1995 (AMT1) the ventilation zone northward limit was farther south (27°S). Differences in atmospheric forcing (surface cooling and wind mixing) are probably the main cause for this interannual variability. In the spring of 1995 the MLD between 25°S and 35°S was much shallower (70–120m) than in the spring of 1999 (120–180m) when vertical mixing was stronger. The shallowest mixed layer depths (~2m) occurred during AMT4, 6B, and 7. These shallow mixed layer depths in spring and fall occurred at the poleward edge (30°S–40°S) of the SASG where there is significant seasonal heating, a large annual range in wind stress, and deep winter mixed layers. The solar heating and reduced wind stirring of spring can cause the upper layer to become thermally restratified, which creates a shallow mixed layer separated from the older, deeper winter mixed layer by a well-stratified thermocline. The very stable waters in the seasonal thermocline isolate the lower isothermal layer and prevent further modification of its properties. Therefore, the deep homogeneous layer (thermostad) retains the water characteristics of its winter formation period and becomes 'fossilized'. This homogeneous layer is called the Subtropical Mode Water (SMW). Studies of the SMW in the North Pacific have shown that the fossilized layers may be subducted into the permanent thermocline via Ekman pumping and transported, retaining their characteristic thermostad, with flow in the subtropical gyre [*Bingham*, 1992; *Hautala and Roemmich*, 1998; *Sprintall and Cronin*, 2001; *Suga et al.*, 1997].

Figure 10 shows meridional transects of XBT temperature and CTD temperature and salinity for spring (AMT1, 3) and fall (AMT2, 4). The XBT data are only available from AMT 1, 2, 3, and 4 cruises. Therefore, only CTD data from those cruises were used for comparison. As previously mentioned, the major distinction between the XBT and CTD temperature transects is the horizontal spatial resolution and the limited CTD sampling depth (200m). The higher horizontal resolution of the XBT transects captures

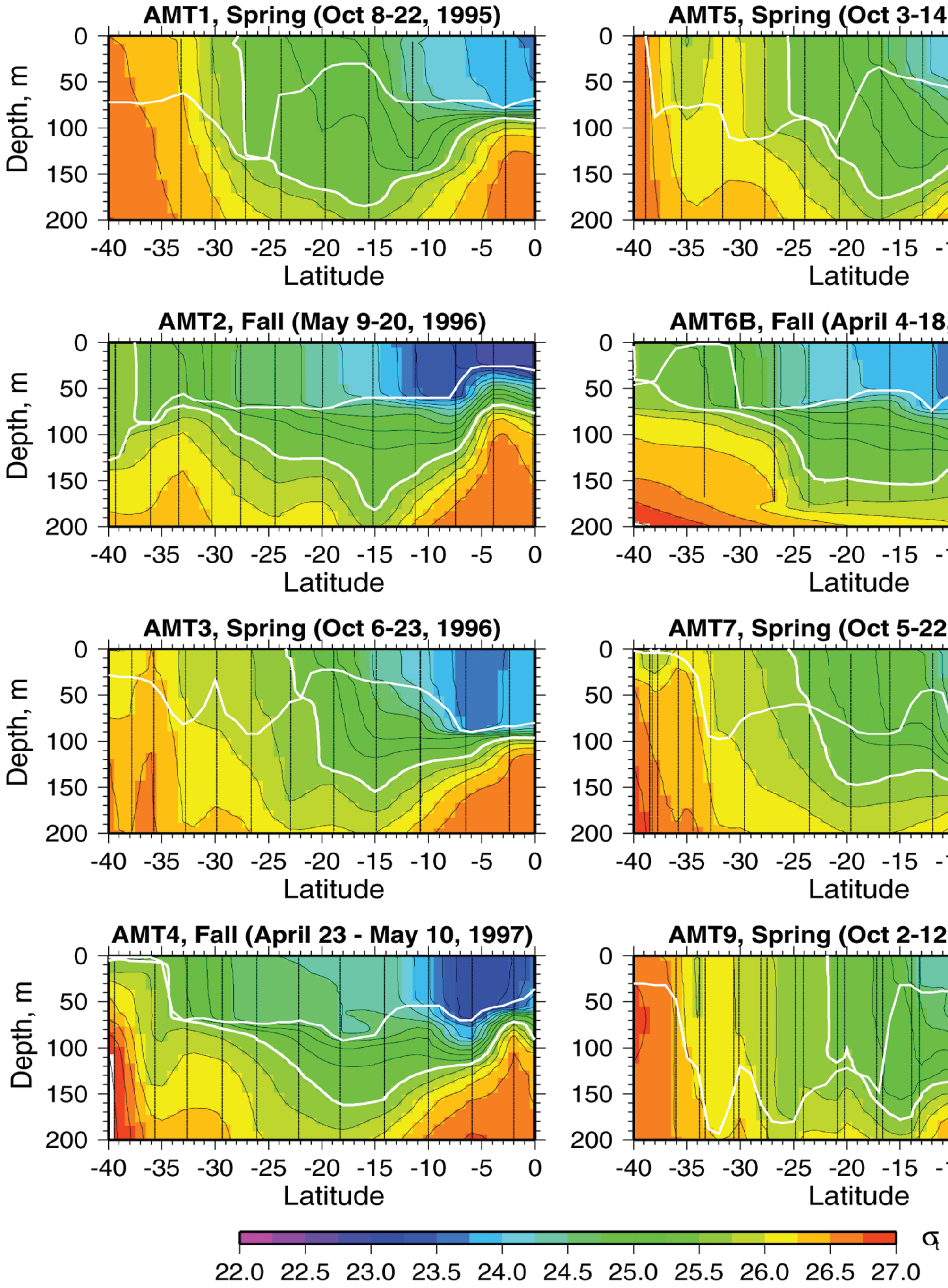

**Figure 9.** Meridional transects of density ($\sigma_t$) obtained from CTD stations during AMT1, 2, 3, 4, 5, 6B, 7 and 9. The thick white line is the pycnocline depth while the thin white line is the mixed layer depth.

the relatively narrow SMW thermostad south of 35°S in both seasons, while the CTD transects miss it entirely during the spring cruises, but partially captures it during the fall cruises. In addition, the MLD (thin white lines) and depth of the 20°C isotherm (Z20, thick white lines) derived from the XBT data have more meridional variability than those derived from the CTD data. The Z20 is a proxy for the thermocline depth. The CTD-derived MLD is based on Equation 1, while the XBT-derived MLD was obtained as the first depth at which the temperature is 0.5°C less than the surface temperature. Note that in spring the MLD inside the gyre (~20°S) obtained from the XBT method is much deeper (150m) than the MLD obtained from the CTD density (30m using Equation 1). This shows the effect of the salinity barrier layer limiting the mixing depth. Within the gyre domain, the MLD is always shallower than the Z20, except in the spring when the Z20 is equal or shallower than the MLD in the subduction zone south of 28°S. Near the gyre center (maximum Z20 at ~15°S), the spring MLD (30m) is shallower than the fall MLD (60m). The mixed layer salinity reaches its maximum near the gyre center where atmospheric moisture divergence reaches its peak. Below the mixed layer salinity and temperature are tightly correlated, as indicated by the similarity between the Z20 and salinity contours.

### *4.2 Penetrating Solar Radiation*

The influence of penetrating solar radiation on the heat budget of the oceans has been a topic of central interest in studies of ocean-atmosphere interactions [*Carter Ohlmann et al.*, 1996; *Gildor et al.*, 2003; *Lewis et al.*, 1990; *Lewis et al.*, 1983; *Murtugudde et al.*, 2002; *Siegel et al.*, 1995]. Solar radiation passes beyond the air-sea interface, and through its vertical divergence can directly heat well below the ocean surface. Solar energy can penetrate beyond the base of the mixed layer, becoming lost to immediate mixed layer heating and further sea-air exchanges. The penetrative component of solar radiation can vary significantly on synoptic to seasonal timescales due to planetary solar cycles, mixed layer evolution, and changes in radiance attenuation due to variations in algal pigment concentrations.

Here, we analyze the meridional variability of penetrating solar radiation based on the AMT spring and fall cruises. The average rate that visible (PAR) solar radiation heats the upper ocean (Radiation Heating Rate, RHR in $^{o}C\ s^{-1}$) of layer thickness equal to the MLD is:

$$\mathrm{RHR(MLD)} = \frac{\mathrm{E_{PAR}(O^{-}) - E_{PAR}(MLD)}}{\rho(\mathrm{MLD})\, c_p\, \mathrm{MLD}} \qquad (1)$$

where, $E_{PAR}(O^{-})$ is the PAR ($W\ m^{-2}$, or $J\ s^{-1}\ m^{-2}$) just below the surface, $E_{PAR}(MLD)$ is the PAR that reaches the MLD (m) , ρ ($kg\ m^{-3}$) is the water density, and $c_p$ (~4100 $J\,kg^{-1}\ {}^{o}C^{-1}$) is the heat capacity of sea water at constant pressure. Solar PAR profiles were obtained along with various CTD casts, so MLD and PAR data are available to calculate RHR (Equation 1). However, PAR profiles were obtained at different times of day (but usually around noon) and different cloudiness conditions throughout all the CTD stations. Therefore, the PAR profiles need to be normalized by the value of $E_{PAR}(O^{-})$ for each profile to obtain a consistent distribution of penetrating radiance along the AMT transects.

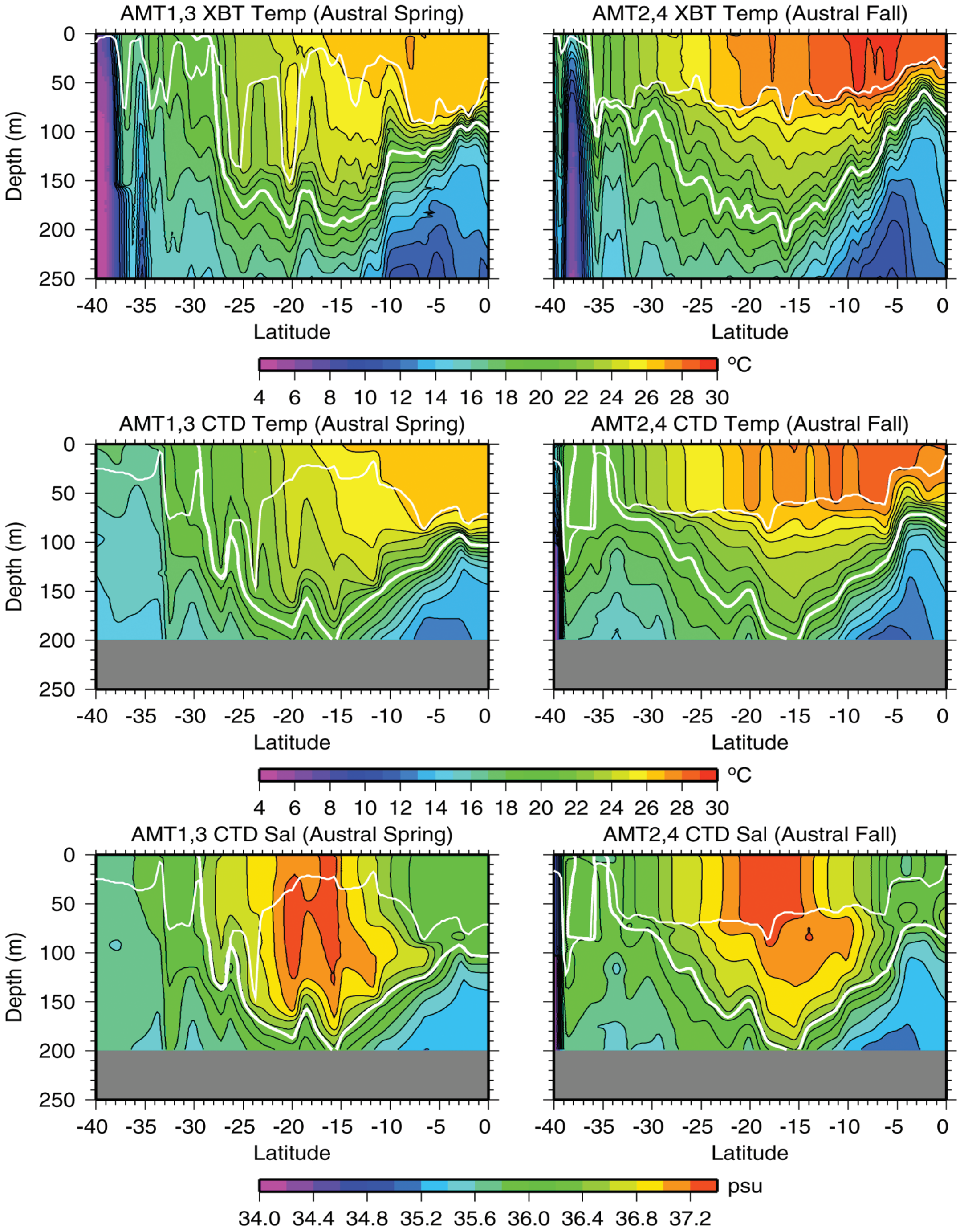

**Figure 10.** Meridional transects of XBT temperature and CTD temperature and salinity for spring and fall. The thick white line is the thermocline depth and the thin white line is the mixed layer depth.

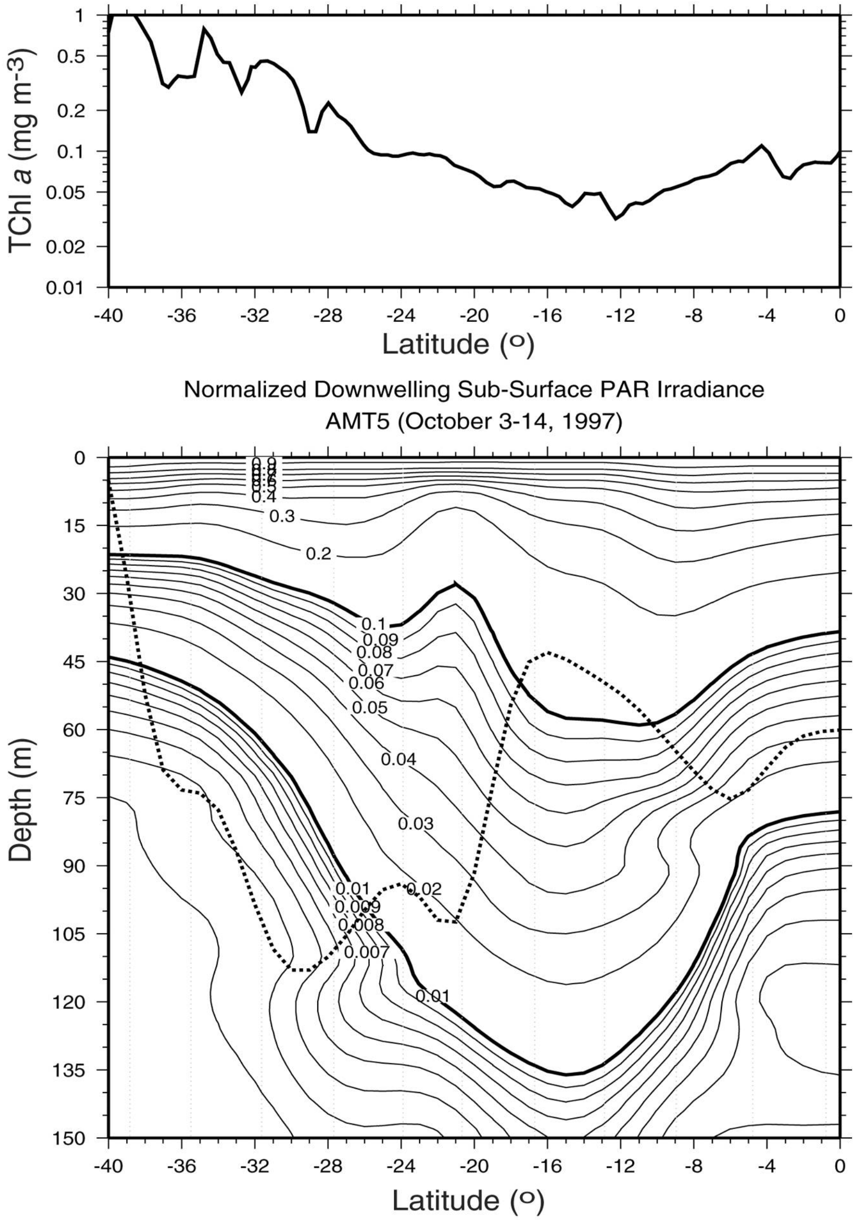

**Figure 11.** Meridional variability of surface chlorophyll (top panel), and normalized downwelling sub-surface PAR irradiance (bottom panel) from AMT-5 stations. The dotted line on the bottom panel is the mixed layer depth in meters. The 0.01 isolume is the $Z_{1\%}$ , or the euphotic zone depth.

Figures 11, 12, and 13 show normalized PAR transects for AMT-5, AMT-6B, and AMT-7, respectively. The MLD is superposed as dotted lines, and the corresponding surface chlorophyll concentration is plotted on top of each transect. During spring of 1997 (AMT-5), at the location of the chlorophyll minimum (~12$^{o}$S), the MLD is shallowest and the solar transmission is largest. At ~30$^{o}$S, the MLD is deepest and solar transmission is significantly reduced due to higher chlorophyll concentration (>0.3 mg m$^{-3}$ ). The amount of light that penetrates below the MLD varies significantly, from 40% at 40$^{o}$S where the MLD is shallowest (5 m), to 0.35% at 30$^{o}$S where the MLD is deepest (110m).

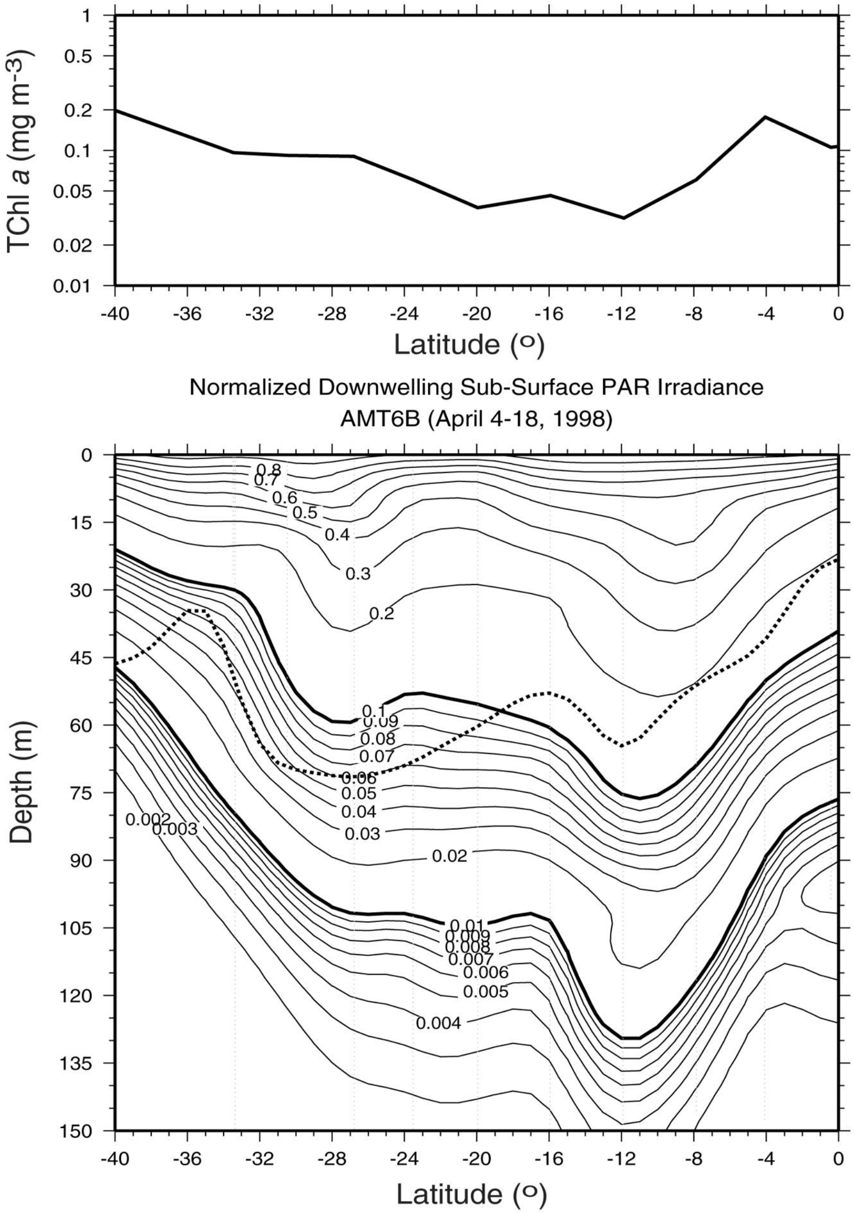

**Figure 12.** Meridional variability of surface chlorophyll (top panel), and normalized downwelling sub-surface PAR irradiance (bottom panel) from AMT-6B stations. The dotted line on the bottom panel is the mixed layer depth in meters. The 0.01 isolume is the $Z_{1\%}$ , or the euphotic zone depth.

In the fall of 1998 (AMT-6B), the PAR penetration and the MLD were in phase, i.e., the solar transmission and RHR increase with the MLD. At 12$^{o}$S, the MLD was 60m, the amount of light that penetrated below it was 15%, and the chlorophyll reached its minimum value (~0.03 mg m$^{-3}$). The maximum MLD was 70m at 28$^{o}$S, where 6% of the surface light penetrated that depth. In the spring of 1998 (AMT-7), the penetrating radiance behaved similar to the conditions found in the spring of 1997 (AMT-5), i.e., the

MLD and solar transmission were in phase opposition. The minimum MLD was 7m at 38°S, where 40% of the surface solar radiation penetrated this depth and the surface chlorophyll concentration was greater than 0.2mg m$^{-3}$. The MLD reached maximum values (85m–90m) at three latitudes, 32°S, 17°S, and 9°S, where 2% of the surface solar radiation penetrated these depths.

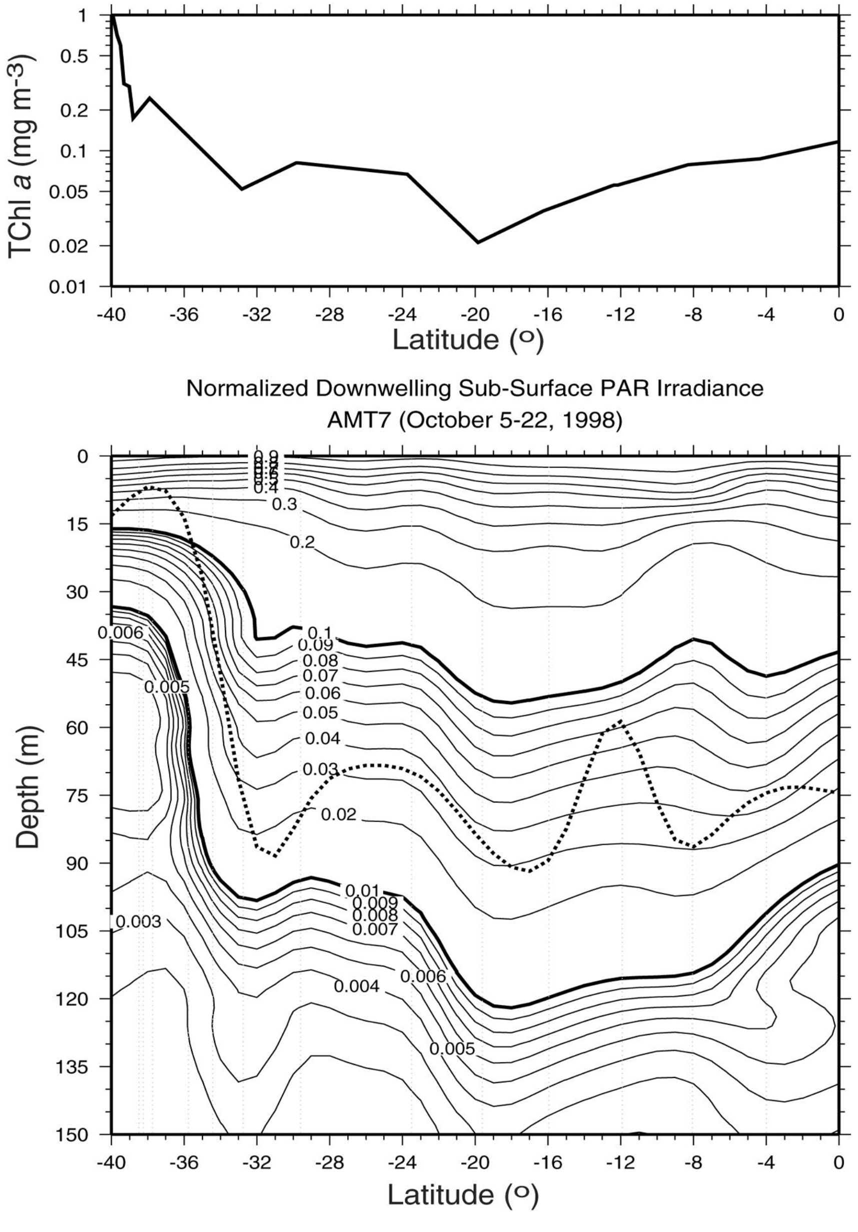

**Figure 13.** Meridional variability of surface chlorophyll (top panel), and normalized downwelling sub-surface PAR irradiance (bottom panel) from AMT-7 stations. The dotted line on the bottom panel is the mixed layer depth in meters. The 0.01 isolume is the $Z_{1\%}$ , or the euphotic zone depth.

The MLDs are larger in spring than fall due to differences in surface heating minus cooling, and differences in the strength of surface winds. The water transparency to visible solar radiation is a function of the chlorophyll concentration. The transparency is lowest in the equatorial and STC regions, and highest at the location of the minimum chlorophyll concentration. The solar radiation that reached the MLD was maximum (40%) in spring near the STC (~40°S) where the MLD was shallowest (5m–7m) and the chlorophyll concentration was relatively large ($>0.3\,\mathrm{mg\,m^{-3}}$), and minimum (<2%) where the mixed layer was deepest (110m) and the chlorophyll concentration was low ($<0.1\,\mathrm{mg\,m^{-3}}$).

### *4.3 Nutrient Distribution*

The meridional transects of nitrate, phosphate, and silicate for spring (AMT1, 3, 5) and fall (AMT2, 4) are shown in Figure 14. The nutriclines for nitrate, phosphate, and silicate are represented by the 2.0 μM, 0.2 μM, and 1.5 μM white contours, respectively. All nutriclines have maximum depths near the gyre center and are deeper during fall than during spring. For example, the nitrate nutricline has a maximum depth of 177m at 20°S in the spring and 191m at 24°S in the fall. This is consistent with the strengthening of the gyre circulation and Ekman downwelling in the fall (Figure 4). During AMT-2 and AMT-3, *Marañón et al.* [2000] found a significant inverse relationship between surface phytoplankton growth and the depth of the nitracline. The location of the deepest nutriclines depends on the criterion used to obtain them, i.e., the first depth at which the nutrients reach a prescribed concentration. For example, for the nitrate transect (top plates in Figure 14) the maximum depth of the 2.0 μM contour (thick white line) is at 20°S, whereas the maximum depth of the 0.1 μM contour (thin white line) is at 17°S. This meridional shift of the contour lines results from the northward tilt of the gyre center towards the surface. In the oligotrophic subtropical gyres, the nitrate uptake rate exceeds the upward diffusive nitrate supply to the biogenic layer [*Planas et al.*, 1999]. This suggests that the nutrients required to support uptake rates measured in the most oligotrophic waters are supplied by other mechanisms. Atmospheric inputs [*Gruber and Sarmiento*, 1997], episodic inputs resulting from mesoscale eddy dynamics [*McGillicuddy et al.*, 1998; *Oschlies and Garçon*, 1998], and Ekman transport from the gyre fringes [*Williams and Follows*, 1998] are the most viable mechanisms contributing to nutrient demand.

### *4.4 Chlorophyll a Distribution*

Figure 15 shows the meridional distribution of TChl *a* in the upper 200 meters for spring and fall. The MLD (thin white line) and the 1% isolume contours (thick white line) are superposed. Due to the sparse data distribution, all the available data from the odd-numbered cruises (AMT-1, 3, 5, 7, 11) were used for the spring chlorophyll transect, while data from the even-numbered cruises (AMT-2, 4, 10) were used for the fall chlorophyll transect. The depth of the maximum TChl *a* concentration follows the depth of $Z_{1\%}$ in the spring, but is shallower than the 1% isolume contour during fall. The chlorophyll concentration peaks during spring in the region of highest nutrient concentration (upper 50m south of 28°S). This is a region where both MLD and $Z_{1\%}$ are shallow (20-65m). The shallowest MLD coincides with the deepest $Z_{1\%}$ and the minimum surface TChl *a* during both spring and fall. This is the location of the clearest and most nutrient-starved waters in the gyre. The deep chlorophyll maximum (DCM) within the gyre lies at the crossover between light and nutrient limitations, and the $Z_{1\%}$ is a good indicator of the DCM depth (see Figure 15). There is indication from along-track flow fields (not shown), that the DCM south of 25°S may be affected by combined northward Ekman drift (~0.2 cm $s^{-1}$) and Ekman downwelling (~2–5 cm $d^{-1}$). This Ekman circulation may transport phytoplankton from the STF along the DCM, but the flow is too weak to unequivocally quantify its effect.

Profiles of TChl *a* are shown in Figure 16 for two seasons and at five degrees of latitude increments from the equator to 35°S. These profiles were extracted from the meridional transects of TChl *a* (Figure 15), which were obtained by gridding the station data with horizontal resolution of 0.25° of latitude and vertical resolution of 1.25m. A 20-point (half-width of 2.5° and 12.5m) gaussian filter was applied to smooth the sparsely distributed data (see data points in Figure 15). From the equator to 25°S, the DCM is generally deeper in the spring (solid lines) than in the fall (dashed lines), and deepest (80-130m) near the gyre center (15°S-20°S) where the surface TChl *a* reaches its minimum. The DCM is not generally a biomass maximum, but the result of an increased TChl *a* to C ratio [*Marañón et al.*, 2000].

## 5. Bio-Optical Properties

### *6.1 Bio-Optical Properties of the Gyre Domain*

The bio-optical regime within the gyre domain, and its equatorward and poleward fringes, is analyzed using light penetration properties of PAR. The meridional variability of the depth of the 10% ($Z_{10\%}$) and 1% ($Z_{1\%}$) light levels, derived from all available PAR data from the AMT cruises, are shown in Figure 17. Transition zones, identified by abrupt changes in the meridional distribution of $Z_{10\%}$ and $Z_{1\%}$, are labeled *a*, *b*, *c*, and *d*. Starting from the poleward side of the SASG, *a* and *c* (30°S–35°S) denote the transition between the oligotrophic (clear) SASG waters and the mesotrophic (darker) waters of the Subtropical Convergence (STC). Some data points at 30°S show an abrupt deepening of the 1% and 10% light levels, indicating water of very clear nature. This coincides with the region where the Brazil Current veers eastward off the coast of South America, which is of tropical origin and depleted in nutrients. On the equatorward side, *d* indicates the transition between the equatorial upwelling regime (darker waters, shallower $Z_{1\%}$) and the downwelling region of the SEC (clear waters, deeper $Z_{1\%}$). This transition zone coincides with the location of the zero curl of the wind stress (see Figure 6). Moving south, the waters of the SEC become more oligotrophic, with the clearest waters located near 15°S where the $Z_{10\%}$ and $Z_{1\%}$ reach maximum depth (~55m and ~120m, respectively). This is the transition zone (*b*) between the SEC and the SASG (see T-S properties in Figure 7). The SASG boundaries are indicated by *b* (15°S) and *c* (30°S) in Figure 17.

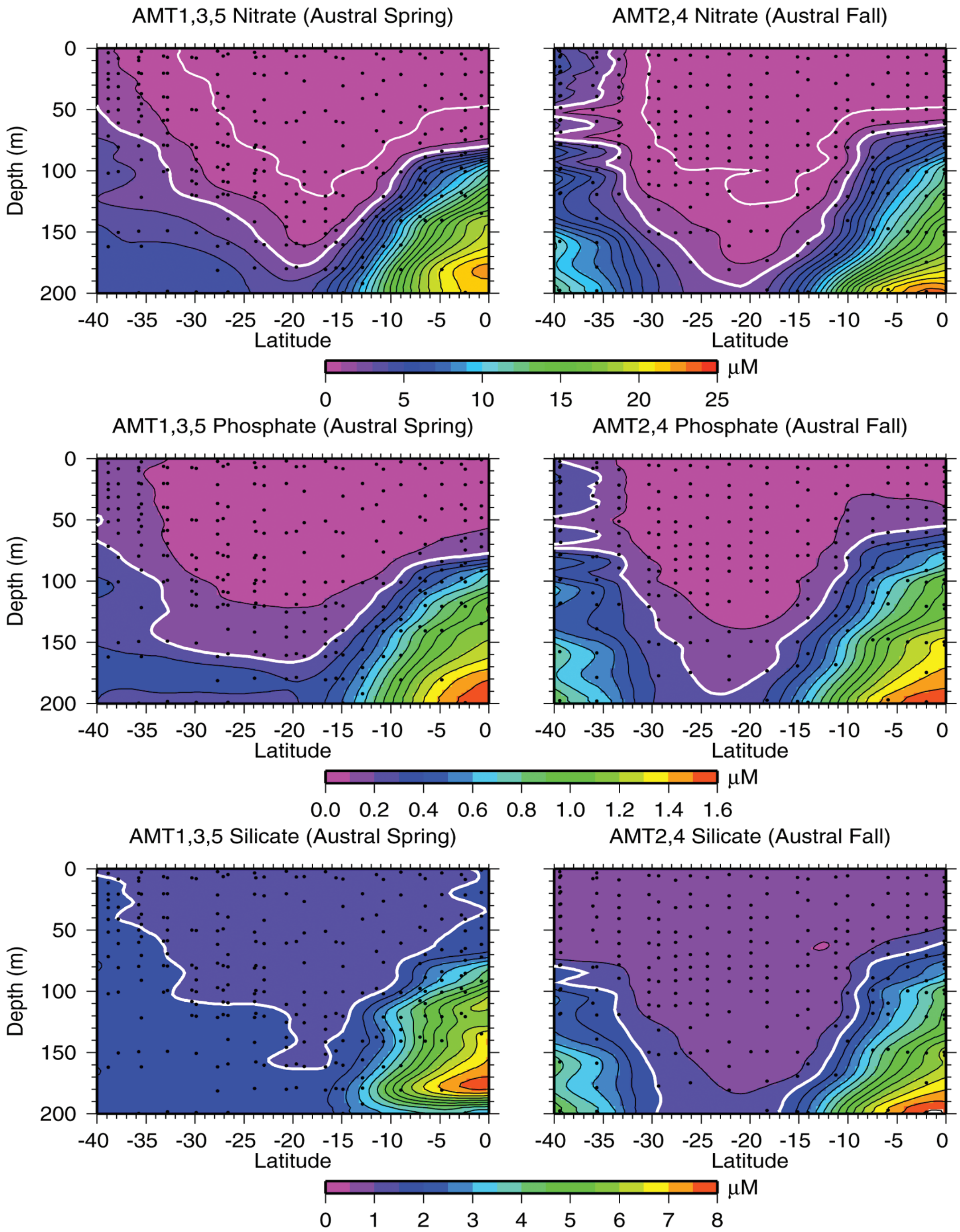

**Figure 14.** Meridional transects of nitrate, phosphate, and silicate for spring and fall. The thick white lines represent the nutricline depths. The thin white lines on the nitrate transects are the 0.1 µM contours.

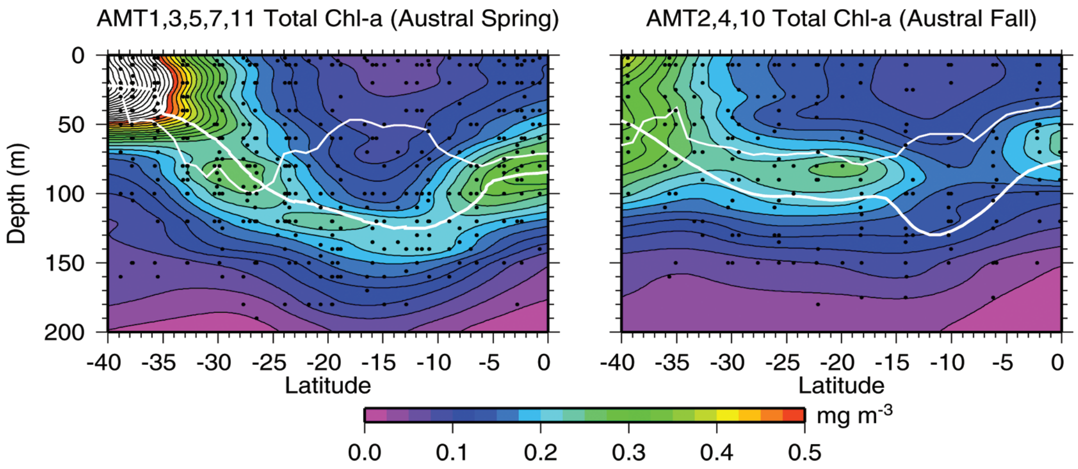

**Figure 15.** Meridional distribution of total chlorophyll *a* for spring and fall. The thick white line is the 1% isolume and the thin white line is the mixed layer depth.

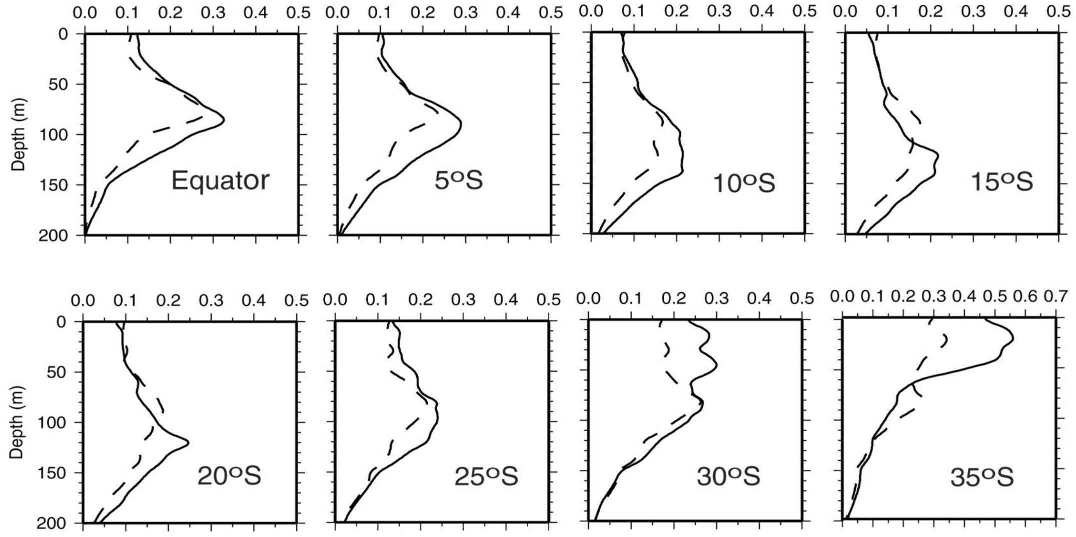

**Figure 16.** Vertical profiles of TChl *a* for spring (solid lines) and fall (dashed lines) at eight selected latitudes.

## *6.2 Relationship between Bio-Optical Properties and Ocean Color Remote Sensing*

### *6.2.1 Total Chlorophyll a*

A comparison of chlorophyll estimated by the SeaWiFS Ocean Chlorophyll 4 version 4 algorithm (OC4v4, [*O'Reilly et al.*, 2000]), using *in situ* measurements of reflectances, and the HPLC chlorophyll measurements, is provided here to demonstrate the robust nature of the algorithm and accuracy of the bio-optical data. The fourth order polynomial equation for the OC4v4 algorithm is:

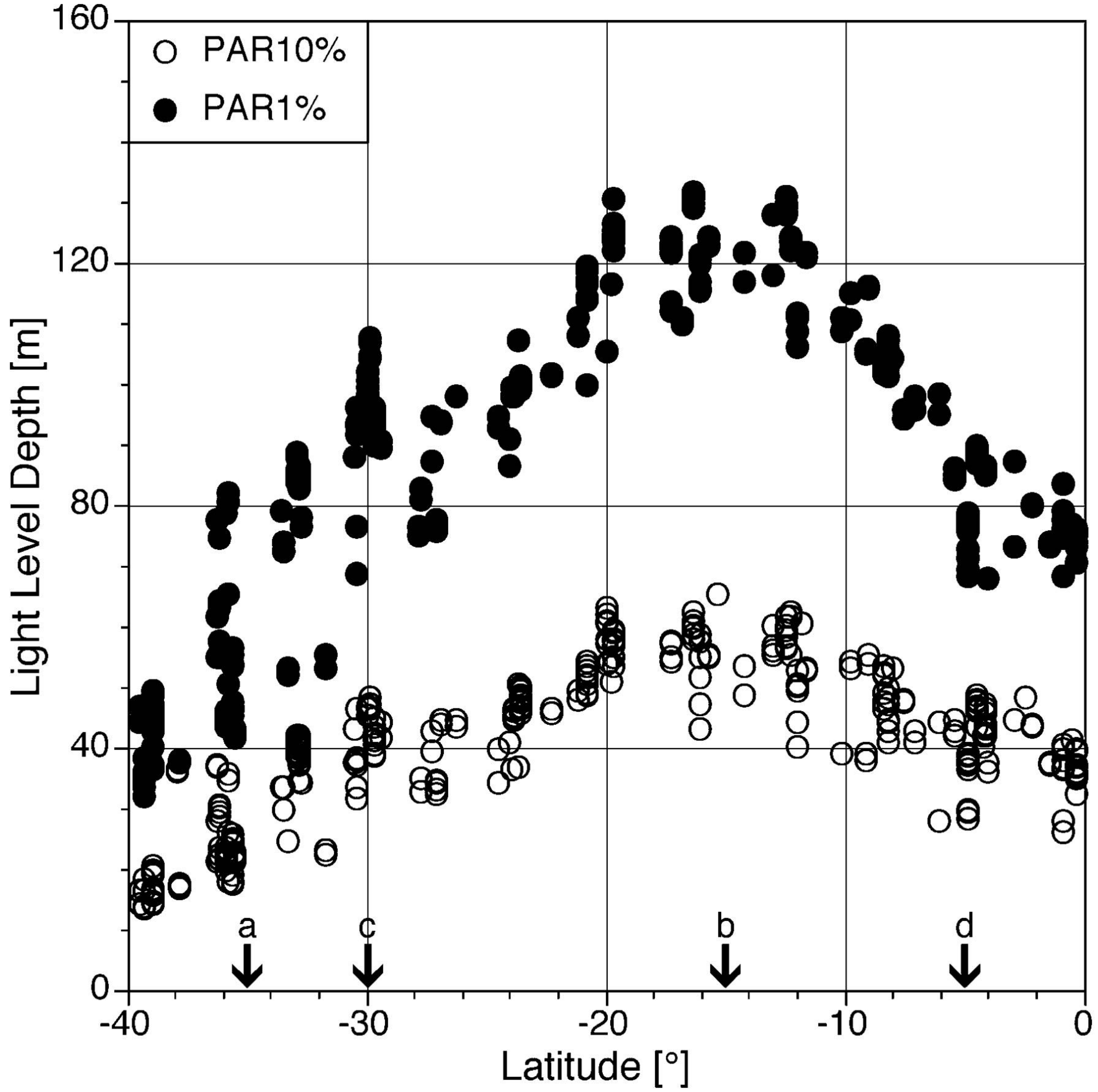

**Figure 17.** Meridional Variability of the depth of the 10% ($Z_{10\%}$) and 1% ($Z_{1\%}$) light levels. Transition zones, identified by abrupt changes in the meridional distribution of the $Z_{10\%}$ and $Z_{1\%}$, are labeled a, b, c, and d (see subsection 6.2).

$$\mathrm{TChl}\,a = 10.0^{(0.366 - 3.067R_{4S} + 1.930R_{4S}^{2} + 0.649R_{4S}^{3} - 1.532R_{4S}^{4})} \quad (2)$$

where TChl $a$ is in mg m$^{-3}$, $R_{4S} = \log_{10}(R_{555}^{443} > R_{555}^{490} > R_{555}^{510})$, and the argument of the logarithm is a shorthand representation for the maximum of the three values, and $R_{\lambda_1}^{\lambda_2}$ represents the remote sensing reflectance ratios at wavelengths $\lambda_1$ and $\lambda_2$.

Figure 18 shows a comparison between the chlorophyll estimated by the OC4v4 algorithm using observed reflectance ratios at the SeaWiFS bands (443, 490, 510, and 555 nm), and the corresponding HPLC-derived chlorophyll values. Only data collected between the equator and 40°S were used in the analysis. The optical data is more abundant than the HPLC-derived chlorophyll, i. e., for each chlorophyll measurement there are multiple observations of reflectance at different times during each station. This is the reason for the vertical stacking of the data points, as exemplified inside the dashed circle in Figure 18. There is a good match between the two methods to derive chlorophyll concentrations. There is no identifiable bias in the scatter plot (data lies evenly distributed around the 1:1 line), except for the low end of the chlorophyll scale where a cluster of values show OC4v4 values twice as high as those from the HPLC method (0.04 and 0.02, respectively). The meridional distribution (0–40°S) of surface chlorophyll, obtained from the two methods described above (OC4v4 and HPLC), is

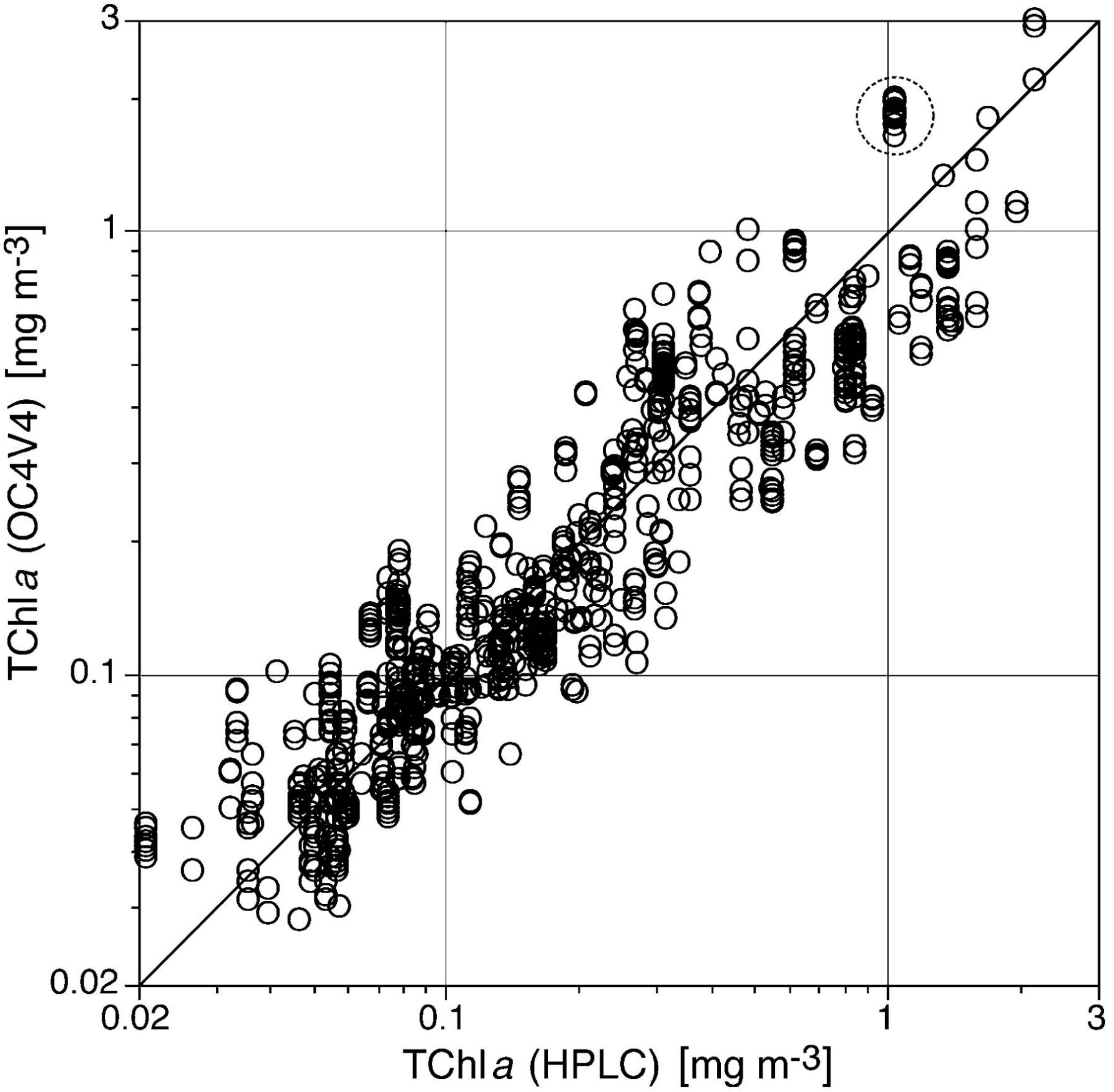

**Figure 18.** Comparison between HPLC-derived Tchl *a* and Tchl *a* from the SeaWiFS OC4v4 algorithm using *in situ* measured reflectances. The dashed circle highlights the "stacking" of data points due to a single TChl *a* measurement paired with several optical measurements (reflectances).

shown in Figure 19. There is good agreement between the data derived from the two methods, and both data sets clearly show the transition zones discussed in subsection *6.1*.

### *6.2.2 Diffuse Attenuation Coefficient*

The SeaWiFS algorithm for the diffuse attenuation coefficient, *K*(490), was used in conjunction with observed normalized water-leaving radiances ($L_{WN}$) at 490 and 555nm to conduct an evaluation of its performance. The values derived with the algorithm were compared with the in situ $K_d(490)$ values. Observed water-leaving radiances and in situ $K_d(490)$ originate from cruises AMT-1 through AMT-8. Data from the entire transects (UK to the Falklands) were used. The SeaWiFS algorithm [*Mueller*, 2000] is given by:

$$K(490) = 0.016 + 0.15645\left[\frac{L_{WN}(490)}{L_{WN}(555)}\right]^{-1.5401} \text{, where } K(490) \text{ is in m}^{-1} \qquad (3)$$

Figure 20 shows a comparison between the *in situ* $K_d(490)$ and the corresponding *K*(490) values derived from the SeaWiFS algorithm. The algorithm performs well for *K*(490) values greater than ~0.035 $\text{m}^{-1}$, but significantly overestimates *K*(490) below that value, i.e., in very clear waters of the oligotrophic SASG. Based on this result, the SeaWiFS diffuse attenuation algorithm should be revisited in the next SeaWiFS reprocessing to improve its performance in oligotrophic waters.

## 7. Seasonal Variability of $p\mathrm{CO_2}$

Subtropical gyre $p\mathrm{CO_2}$ can be fairly well reproduced using SST data [*Lefevre and Taylor*, 2002; *Nelson et al.*, 2001]. Using a combination of a one-dimensional ecosystem model and observations from ships of opportunity, *Lefèvre and Taylor* [2002] developed $p\mathrm{CO_2}$-SST relationships for the North Atlantic and South Atlantic subtropical gyres. Data from AMT-2,7 (west side of the gyre) and *St. Helena* (east side of the gyre) cruises were used for the SASG $p\mathrm{CO_2}$-SST relationship. *Lefèvre and Taylor* [2002] constructed an algorithm including SST, latitude, longitude and atmospheric $p\mathrm{CO_2}$ for two periods, one from February to July and another from August to January. We used the SASG algorithm to analyze the seasonal variability of $p\mathrm{CO_2}$ in the region. The two relationships for the SASG, with multiple regression coefficient r=0.99 and valid for the region within the points 35°W, 10°S; 10°W, 10°S; 0°W, 30°S; 35°W, 30°S (shown in Figures 21, 22, and 23), are:

From 1 March to 31 July:

$$p\mathrm{CO_2} = 14.07\times\mathrm{SST} - 1.60\times\mathrm{Lat} + 1.54\times\mathrm{Long} + 0.78\times\mathrm{Atm\_}p\mathrm{CO_2} - 258.49 \qquad (3)$$

From 1 August to 29 February:

$$p\mathrm{CO_2} = 13.74\times\mathrm{SST} - 1.66\times\mathrm{Lat} + 1.57\times\mathrm{Long} + 0.84\times\mathrm{Atm\_}p\mathrm{CO_2} - 267.81 \qquad (4)$$

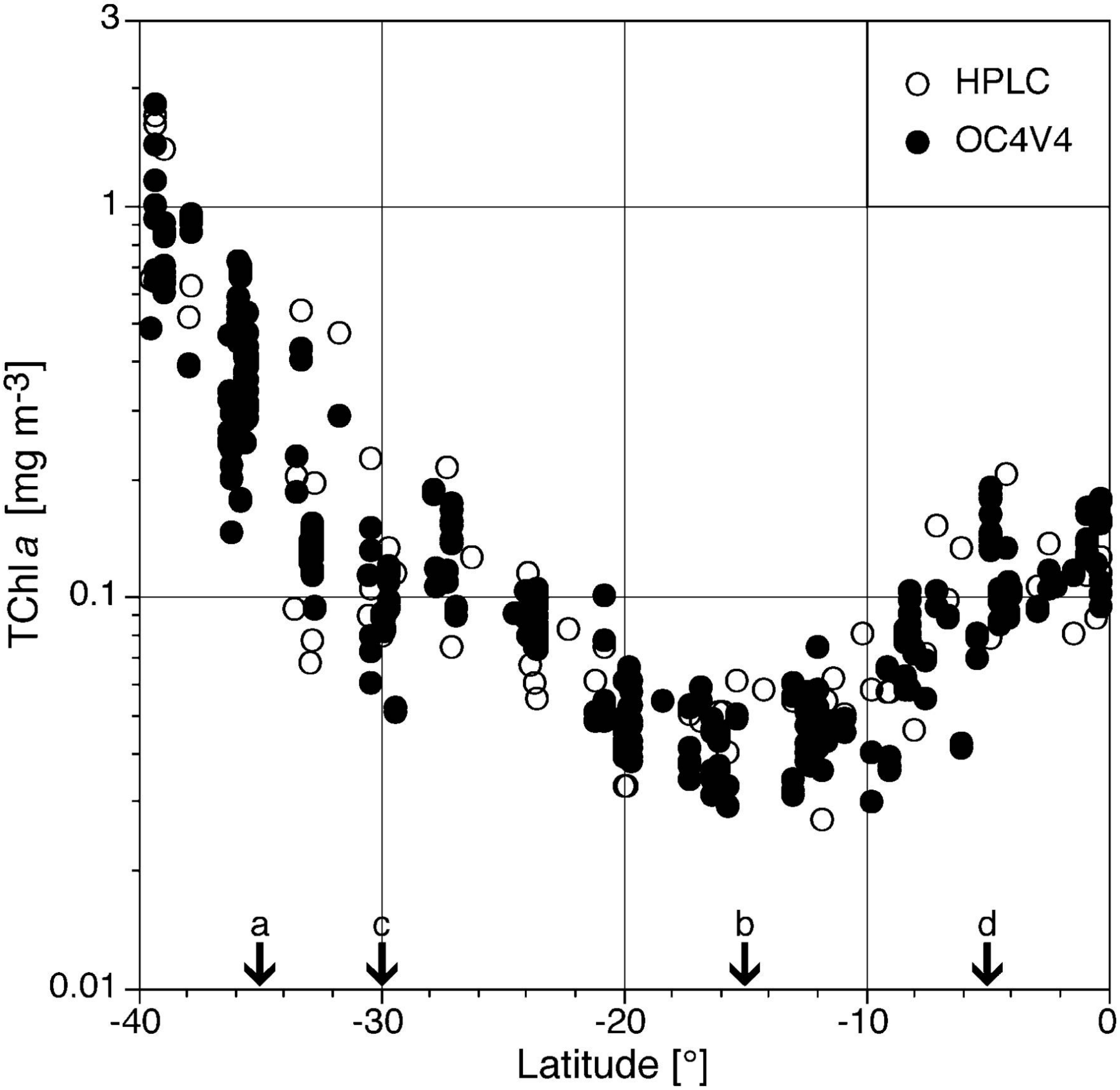

**Figure 19.** Meridional distribution of surface TChl *a*. The white circles indicate values obtained with the HPLC method, while the black circles show the TChl *a* derived from the OC4v4 algorithm using in situ reflectances. The transition zones, defined by abrupt changes in TChl *a*, are labeled a, b, c, and d.

*Lefèvre and Taylor* [2002] compared estimates of $p\text{CO}_2$ derived with Equations 3 and 4 along the AMT and *St. Helena* transects with the underway $p\text{CO}_2$ measurements. The model generally predicts the latitudinal trend for each transect, but systematic biases are evident for AMT-2 (-20 µatm) during May 1996, and *St. Helena* for April (+5 µatm) and June (+3 µatm) 1995. There is no algorithm bias for AMT-7 (October 1995). *Lefèvre and Taylor* [2002] suggest that a possible explanation is the scarcity of data in the SASG and repeated transects at a more central location are needed to determine if a more robust algorithm can be constructed for the region. To improve the model predictability, we applied a bias correction to Equations 3 and 4. At the westernmost longitudes, the correction is –20 µatm in May and zero in October. A linear interpolation provided the bias values for the other months. A linear correction was applied west to east to account

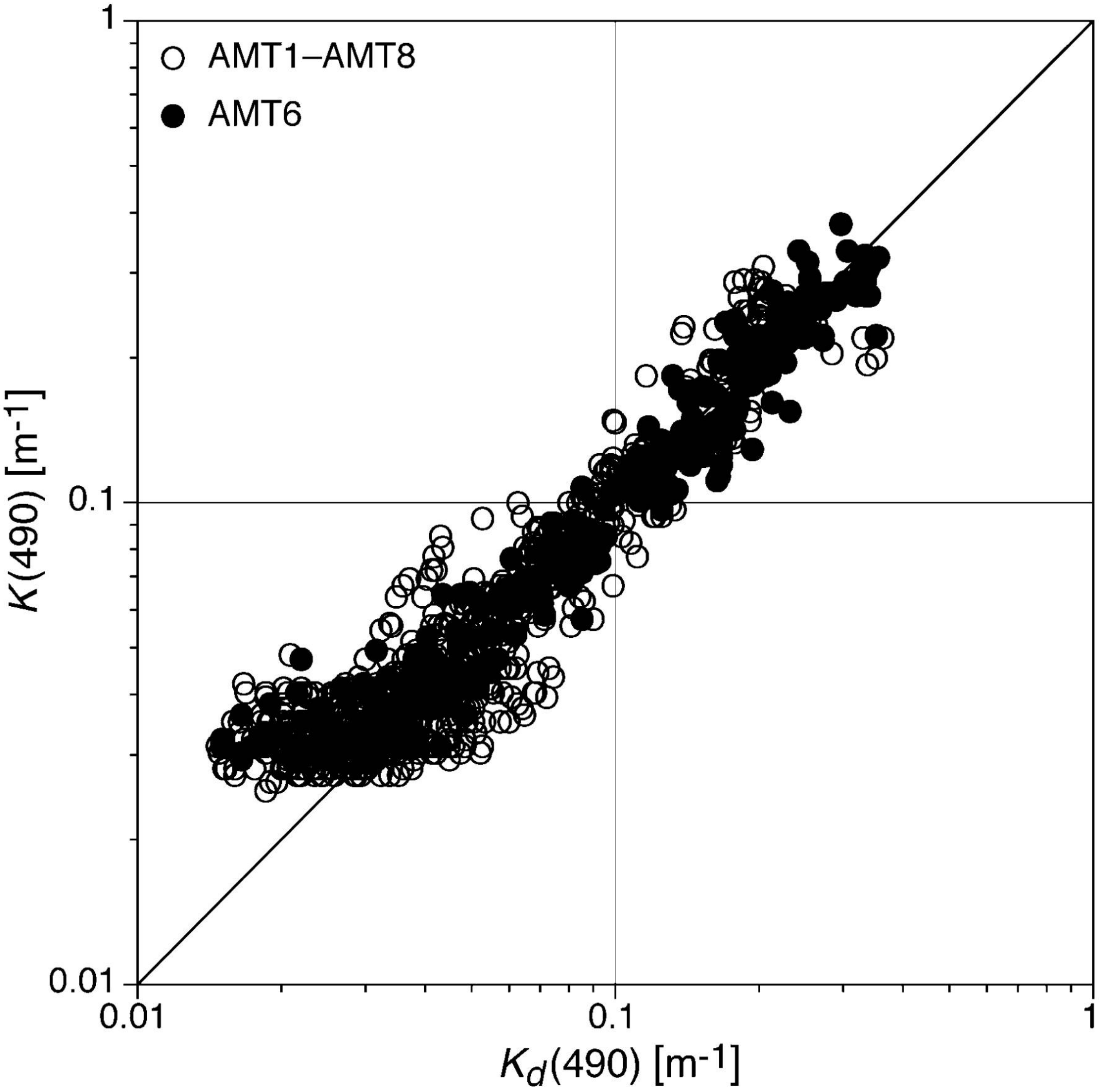

**Figure 20.** Scatter plot of in situ ($K_d$(490)) versus algorithm-derived ($K$(490)) diffusion attenuation coefficients. The blank circles were derived from reflectances measured on cruises AMT-1, 2, 3, 4, 5, 7, and 8, while the filled circles were derived from reflectances measured on AMT-6 only.

for the zonal variability of the $p$CO$_2$ bias. The total bias correction (ε) as a function of month (mo) and longitude is:

$$\varepsilon(\mathrm{mo,lon}) = \varepsilon_{\mathrm{w}}(\mathrm{mo}) + [\varepsilon_{\mathrm{e}}(\mathrm{mo}) - \varepsilon_{\mathrm{w}}(\mathrm{mo})]\frac{[\mathrm{lon} - \mathrm{lon}_{\mathrm{w}}]}{[\mathrm{lon}_{\mathrm{e}} - \mathrm{lon}_{\mathrm{w}}]} \tag{5}$$

where the subscripts w and e denote the west and east transect locations.

A continuous time series of $p$CO$_2$, from July 7, 1991 through December 31, 2001, was constructed using Equations 2 and 3, and weekly SST and interpolated atmospheric $p$CO$_2$ data. The predicted $p$CO$_2$ was corrected using Equation 5. Seasonal $\Delta p$CO$_2$

(Atm_$p\text{CO}_2$ – $p\text{CO}_2$) averages for summer (Dec 1 – Feb 29), fall (Mar 1 – May 31), winter (June 1 – August 31), and spring (September 1 – November 30) were computed for the 10 year period (1992-2001). The seasonal surface distributions of sea-air $\Delta p\text{CO}_2$ are shown in Figure 21. The polygon superposed on the seasonal $\Delta p\text{CO}_2$ distributions delimits the region for which the $p\text{CO}_2$-SST algorithm is valid, which is the region defined as the SASG by *Lefèvre and Taylor* [2002]. This region excludes the Benguela and Brazil currents.

The seasonal cycle of $\Delta p\text{CO}_2$ in the SASG is large. During the austral summer and fall, when SST is warmest, the SASG is oversaturated, with $\Delta p\text{CO}_2$ values as large as 35 µatm. The southwest corner of the region begins to undersaturate during fall with $\Delta p$CO2 values of -15 to –5 µatm. During winter and spring, the SST drops by ~4°C on average and the region becomes undersaturated with $\Delta p\text{CO}_2$ values ranging from 0 in the northern boundary to –60 µatm in the southern boundary. *Lefèvre and Taylor* [2002] compared the $p\text{CO}_2$-SST relationships from the algorithm and observations in the SASG with those deduced from the $\text{CO}_2$ climatology of *Takahashi et al.* [1997] by *Lee et al.* [1998]. From May to August, SST decreases in the gyre and the corresponding increase of $p\text{CO}_2$ found by *Lee et al.* [1998] disagrees with the algorithm and the observations, both of which show a $p\text{CO}_2$ decrease. *Lefèvre and Taylor* [2002] attribute the

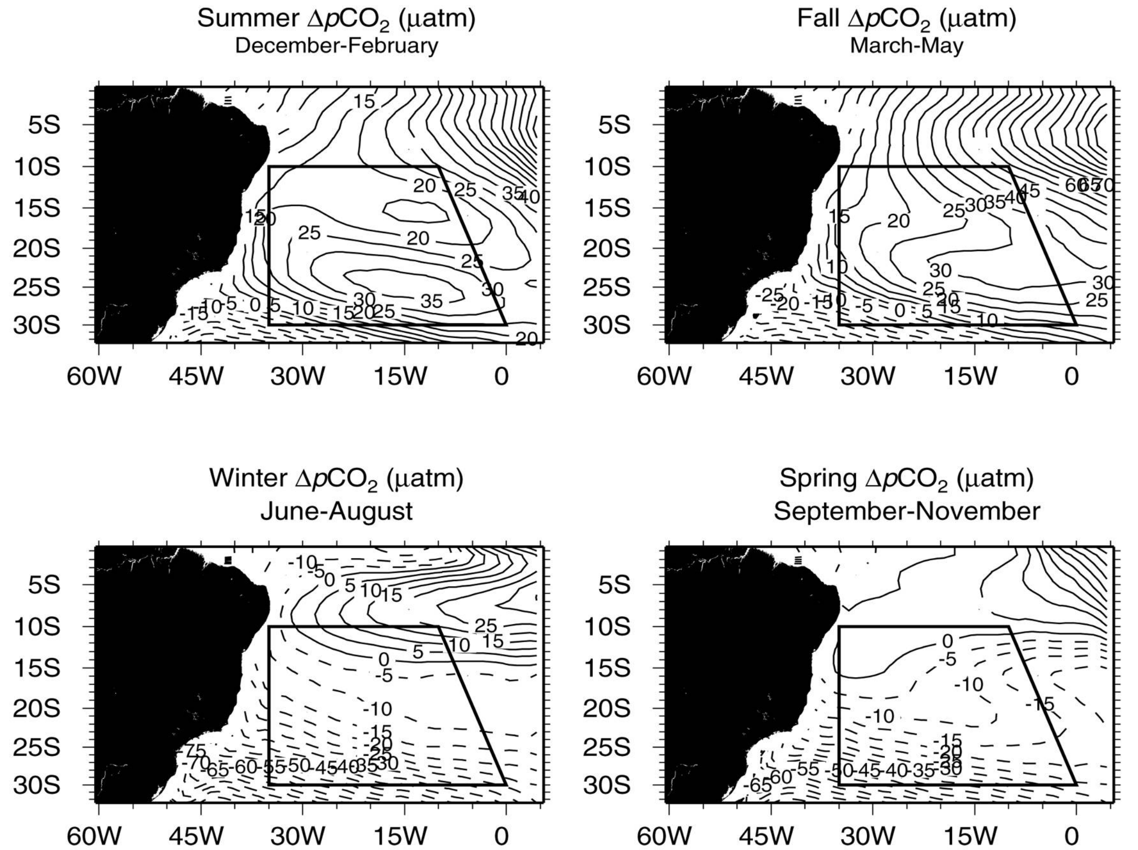

**Figure 21.** Seasonal maps of $\Delta p\text{CO}_2$ predicted with the algorithm of *Lefevre and Taylor* [2002]. The region within which the algorithm is valid is shown by the superposed polygon.

disagreement with *Lee et al.* [1998] to their shortage of data in the SASG and the method used to produce the climatology.

## 8. Sea-Air $CO_2$ Flux

A continuous time series of sea-air $CO_2$ flux was constructed using the $\Delta p\mathrm{CO}_2$ time series derived from the $p\mathrm{CO}_2$-SST algorithm, and 5-day SSM/I winds interpolated to the central times of the weekly SST data. The sea-air $CO_2$ flux, F (mol C $m^{-2}$ $yr^{-1}$), was calculated according to:

$$\mathrm{F} = \mathrm{K_o}\, k\, \Delta p\mathrm{CO_2} \qquad (6)$$

where $K_o$ is the $CO_2$ solubility (mol $kg^{-1}$ $atm^{-1}$), $k$ is the transfer velocity for $CO_2$ sea-air exchange. Solubility was calculated according to *Weiss and Price* [1980], using the Reynolds SST fields and monthly climatological salinities from the World Ocean Atlas 1998 [*Conkright et al.*, 1998]. Following *Wanninkhof* [1992], weekly transfer velocities (cm $h^{-1}$) were computed according to:

$$k = 0.31\mathrm{U}_{10}^{2}\left(\frac{\mathrm{Sc}}{660}\right)^{-\frac{1}{2}} \qquad (7)$$

where $\mathrm{U}_{10}$ is the 10-m SSM/I wind speed and Sc is the Schmidt number computed according to *Wanninkof* [1992] from the Reynolds SST fields.

Mean seasonal maps of wind speed and sea-air $CO_2$ flux are shown in Figures 22 and 23, respectively. Mean wind speeds do not vary significantly from season to season, but there is some meridional variability. They range from 5 m $s^{-1}$ in the southernmost part of the SASG to 7-8 m $s^{-1}$ in the northernmost part (Figure 22), which is the region of the trade winds. The seasonal maps of sea-air $CO_2$ flux (Figure 23) show a pattern very similar to the seasonal distribution of $\Delta p\mathrm{CO}_2$ (Figure 21). Outgassing occurs in summer and fall when the ocean is oversaturated, and ingassing occurs in winter and spring during the undersaturation period. Maximum outgassing occurs during fall with warmest SSTs, while the maximum ingassing occurs in winter-spring when SSTs are coldest. Time series of SST, $p\mathrm{CO}_2$, $\Delta p\mathrm{CO}_2$, wind speed, and sea-air $CO_2$ flux for the period of July 7, 1991 to December 31, 2001, are shown in Figure 24. The SST [*Reynolds and Smith*, 1994] and wind speed (SSM/I) are observed values, while the $p\mathrm{CO}_2$, $\Delta p\mathrm{CO}_2$, and sea-air flux are predictions using the algorithms. The time series were obtained from area averages for each parameter, calculated for the SASG region defined in Figures 21, 22, and 23. A distinct SST seasonal cycle is evident with warmest temperatures in February-March and coldest temperatures in August-September. The seasonal cycle of SST is in phase with the $p\mathrm{CO}_2$, $\Delta p\mathrm{CO}_2$, and sea-air flux seasonal cycles.

The secular trend is superposed on the $p\mathrm{CO}_2$ time series. The ocean $p\mathrm{CO}_2$ secular trend of 1.55 μatm $yr^{-1}$ is not significantly manifested on the $\Delta p\mathrm{CO}_2$ time series as the ocean and atmosphere are in equilibrium at the slow rate of change of the secular trend. Some interannual variability is noticeable in the SST record, and consequently imparted on the $\Delta p\mathrm{CO}_2$. For instance, the coldest summer SSTs occurred in 1997, which caused the lowest $\Delta p\mathrm{CO}_2$ of the entire record. However, the interannual changes seen in the sea-air flux record are mainly caused by wind speed variability from year to year. This is a consequence of the higher frequency variability on the wind speed record, and the quadratic wind-speed dependence of the sea-air flux.

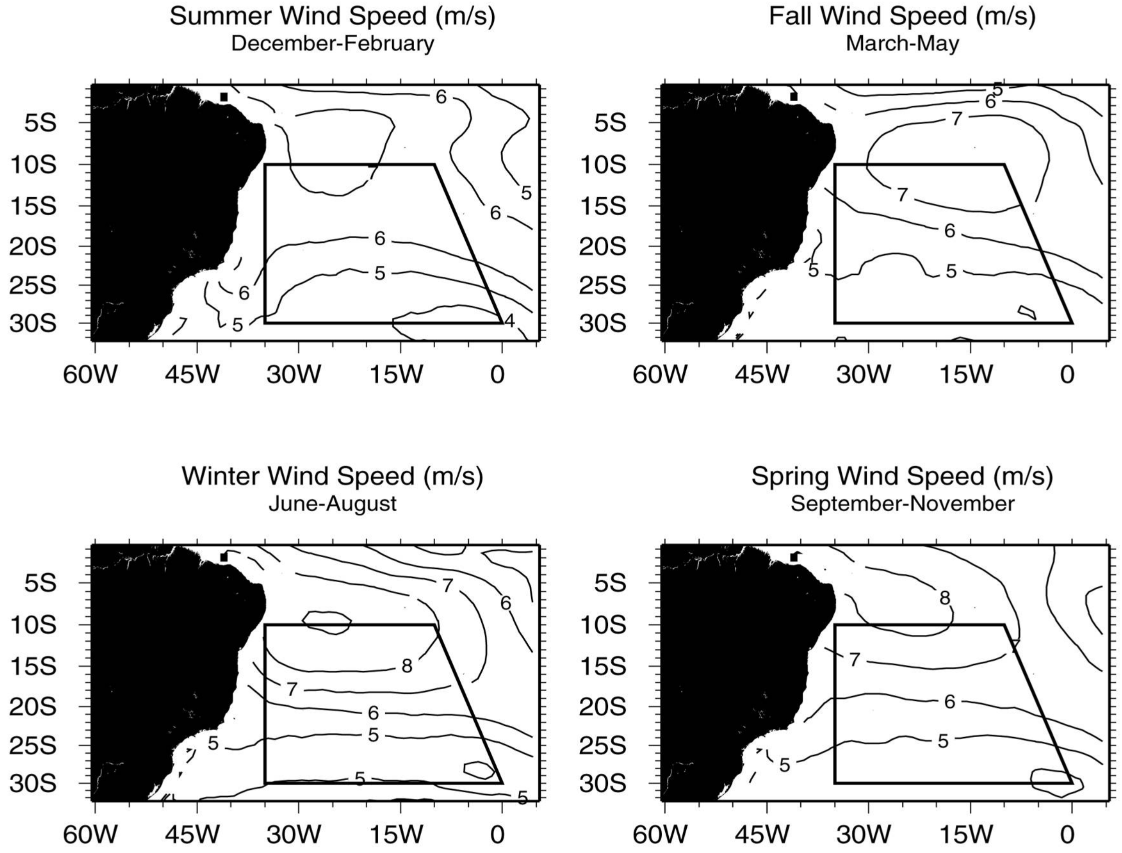
Summer Wind Speed (m/s)
December-February

Fall Wind Speed (m/s)
March-May

Winter Wind Speed (m/s)
June-August

Spring Wind Speed (m/s)
September-November

**Figure 22.** Seasonal maps of wind speed. The region within which the algorithm is valid is shown by the superposed polygon.

The net sea-air $CO_2$ flux for 1992-2001 is +0.014 mol C $m^{-2}$ $yr^{-1}$, or +0.001 Gt C $yr^{-1}$. Therefore, the SASG is a very weak source of carbon, in contrast with estimates for the North Atlantic subtropical gyre (NASG), which is a net sink of carbon with an annual uptake of –0.04 Gt C [*Nelson et al.*, 2001]. The net uptake of carbon in the NASG can be explained by colder winter SSTs when compared to the SASG. Using the NASG boundaries of *Lefèvre and Taylor* [2002] and weekly Reynolds SSTs, the mean 1992-2001 winter SST is 21.6°C, which is about 1°C colder than the SASG mean winter SST of 22.7°C. At a $p\mathrm{CO}_2$-SST sensitivity of 4%/°C [*Lefevre and Taylor*, 2002] and a mean winter $p\mathrm{CO}_2$ of 346 µatm, the 1°C translates into –14 µatm. Therefore, at the SSTs of the NASG, the SASG would be much more undersaturated in winter and very likely become a net sink of carbon. In addition, based on the SSM/I winds, the mean squared winter speeds are slightly higher in the NASG ($U_{10}^2$=42.5 $m^2/s^2$) than they are in the SASG ($U_{10}^2$=41.5 $m^2/s^2$), which is another source for the difference.

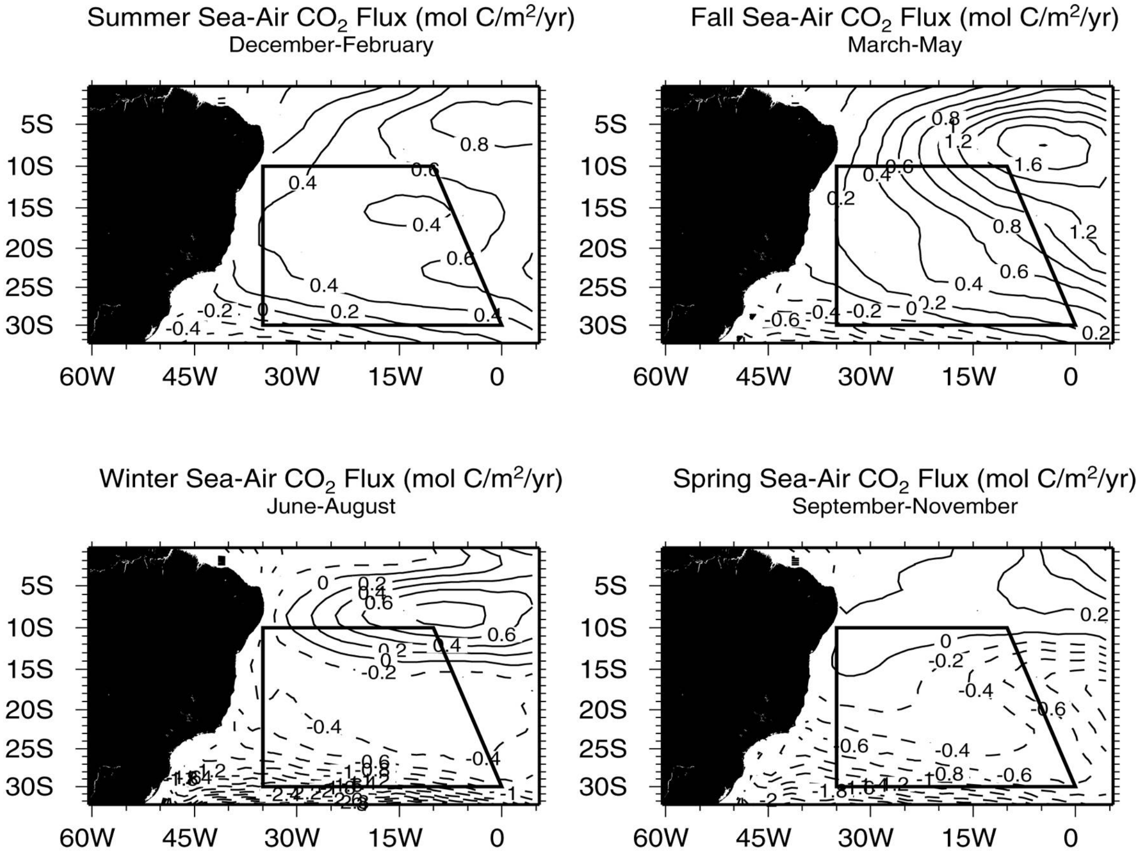

**Figure 23.** Seasonal maps of sea-air $CO_2$ flux predicted with the $pCO_2$ algorithm of *Lefevre and Taylor* [2002] and the gas exchange algorithm of *Wanninkhof* [1992]. Positive fluxes are towards the atmosphere (outgassing).

A third possible source for the difference is the larger atmospheric $pCO_2$ in the North Atlantic. Based on the meridional interpolation of three long-record stations, Cold Bay (50°N), Mauna Loa (19.5°N), and South Pole (90°S), the annual atmospheric $pCO_2$ concentrations at 28°N and 28°S, near the coldest SSTs of the gyres (near the subtropical fronts) where ingassing is largest, are 354.4 μatm and 352.9 μatm, respectively. Therefore, the atmospheric $pCO2$ at 28°N is 1.5 μatm higher than the atmospheric $pCO_2$ at 28°S, which may contribute to the sign difference between the sea-air flux of the two gyres. The peak-to-peak seasonal variability of the atmospheric $pCO_2$ is also larger in the NASG. At 28°N the peak-to-peak variability is 5.7 μatm, while at 28°S it is 3.7 μatm [*Signorini and McClain*, 2002]. However, the higher SST (difference of 1°C) in the NASG has a much larger effect on the sea-air flux via the 14 μatm reduction in ocean $pCO_2$, than the 1.5 μatm difference in atmospheric $pCO_2$ between the two gyres.

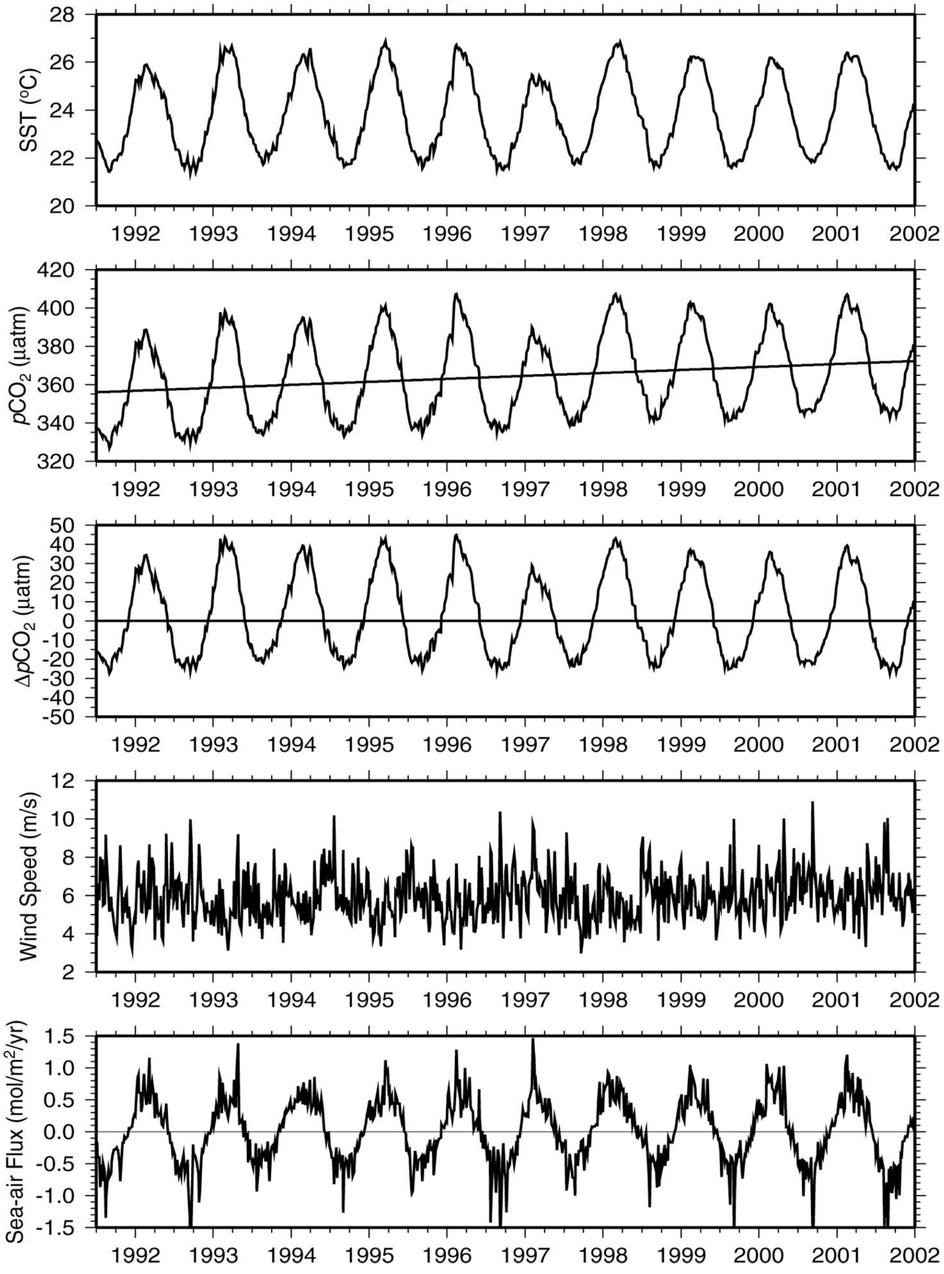

**Figure 24.** Time series of weekly SST (Reynolds and Smith, 1994), predicted $p$CO$_2$ and $\Delta p$CO2, SSM/I wind speed, and predicted sea-air CO$_2$ flux. The line on the $p$CO$_2$ time series is the secular trend.

## 9. Summary and Conclusions

Hydrographic, nutrient, pigment, and optical in situ data from AMT cruises, in conjunction with SeaWiFS ocean color data, were used to characterize the biogeochemical boundaries, the phytoplankton communities, and the bio-optical properties of the SASG. Chlorophyll values measured with the HPLC method were compared with those obtained from measured reflectances and the use of the OC4v4

SeaWiFS algorithm. A $p\mathrm{CO}_2$-SST algorithm [*Lefevre and Taylor*, 2002] was used to analyze the seasonal variability of $\Delta p\mathrm{CO}_2$ and sea-air $\mathrm{CO}_2$ flux in the SASG. The main results of our study may be summarized as follows.

- The gyre boundaries were determined by a combination of water mass analysis, dynamics of the major currents, and meridional bio-optical gradients. The meridional extent of the SASG lies between 15°S and 30°S.

- The waters of the central SASG are characterized by a deep pycnocline (140−180m) and nitracline (180−190m), warm SSTs (>24°C) and high SSS (>37.0), mixed layer depths shallower by 50−80m than the nitracline, and nitrate (0−0.1 μM) and phosphate (0−0.1 μM) concentrations mostly below detection near the surface. The silicate concentration near the surface (0.3−1.7 μM) is relatively high, indicating that phytoplankton growth in the central SASG is mostly phosphate and nitrate limited. The deepest euphotic zone depth is 130m. The average surface chlorophyll concentration is low (0.07 mg $\mathrm{m}^{-3}$) and the DCM is deep (80m−130m).

- The circulation of the SASG is closed in the south by the South Atlantic Current (SAC). The eastward-flowing SAC is distinct from the Antarctic Circumpolar Current, and is separated from it by the Subtropical Front (STF) [*Peterson and Stramma*, 1991]. At the longitude of the AMT cruises the STF is located near 40°S. Between 30°S–40°S, the pycnocline and nitracline outcrop to the surface, the mixed layer and euphotic zone depths are shallower by 20−60m than at the gyre's center, and the nutrient ($\mathrm{NO}_3$=2.1 μM, $\mathrm{PO}_4$=0.2 μM, $\mathrm{SiO}_2$=1.1 μM) and chlorophyll (0.5 mg $\mathrm{m}^{-3}$) average concentrations in the upper 50m are characteristic of mesotrophic waters.

- The SASG is bounded to the north by the southern branch of the South Equatorial Current (SEC). Near 30°W and 10°S, an area sampled by the AMT cruises, the SEC bifurcates into the northwestward-flowing North Brazil Current (~2/3 of the transport), and the southward-flowing Brazil Current (~1/3 of the transport) [*Stramma et al.*, 1990]. Below 100m, the SEC region is identifiable by the strong subsurface meridional gradients of temperature and salinity between 5°S–15°S. Above the thermocline (~100m), there is a pool of warm equatorial water with temperatures within 26-28°C. The MLD ranges from 20m in the fall to 80m in the spring. Within this latitude band, the nutrient concentrations for $\mathrm{NO}_3$, $\mathrm{PO}_4$, and $\mathrm{SiO}_2$, with averages of 7.8 μM, 0.7 μM, and 3.2 μM between 100–200m, have meridional gradients coherent with T and S. The equivalent $\mathrm{NO}_3$, $\mathrm{PO}_4$, and $\mathrm{SiO}_2$ average concentrations within the upper 100m are 0.04 μM, 0.09 μM, and 0.88 μM, respectively. The average surface chlorophyll for this region is 0.07 mg $\mathrm{m}^{-3}$ and the DCM ranges from 70 to 120m, which is a response to low nitrate and phosphate concentrations in the euphotic zone (90–130m) imposed by the limited vertical mixing (MLD=20–80m).

- A comparison between the chlorophyll estimated by the OC4v4 algorithm, using observed reflectance ratios at the SeaWiFS bands (443, 490, 510, and 555 nm), and the corresponding HPLC-derived chlorophyll values, revealed that there is no identifiable bias between the OC4v4 algorithm and the data. However, a bias was identified in very clear water between the measured diffuse attenuation coefficient at 490nm ($K_{490}$), and the corresponding $K_{490}$ values from the SeaWiFS algorithm, with the measured values being lower than the algorithm between the equator and 24°S.

- The penetrating solar radiation is a function of MLD and chlorophyll concentration. The MLDs are larger in spring than fall due to differences in surface heating minus cooling, and differences in the strength of surface winds. The water transparency to visible solar radiation is a function of the chlorophyll concentration. The transparency is lowest in the equatorial and STC regions, and highest at the location of the minimum chlorophyll concentration. Solar penetration is maximum (40%) in spring near the STC (~40°S) where the MLD is shallowest (5m–7m) and the chlorophyll concentration is relatively large ($>0.3\,\mathrm{mg\,m^{-3}}$), and minimum (<2%) where the mixed layer is deepest (110m) and the chlorophyll concentration is small ($<0.1\,\mathrm{mg\,m^{-3}}$). Thus the highest penetration radiation is not coincident with the lowest TChl *a* concentrations.

- The seasonal cycle of sea-air $\Delta p\mathrm{CO_2}$ is quite large in the SASG (-25 to +45 μatm), but the mean sea-air $CO_2$ flux is small (+0.014 mol C $m^{-2}$ $yr^{-1}$). There is a significant contrast between the North Atlantic and South Atlantic gyres. While the North Atlantic gyre is a net sink of carbon with an annual uptake of –0.04 Gt C [*Nelson et al.*, 2001], the South Atlantic gyre is a weak source of carbon with an annual outflow of +0.001 Gt C. Colder winter SSTs and stronger winds in the North Atlantic gyre are the main reason for the difference.

## *Acknowledgements*

We wish to acknowledge the NASA Ocean Biogeochemistry Program for funding the data analysis for this study. The in situ optical and pigment data used in this study could not have been collected without the competent contributions of the AMT Principal Scientists and the *RRS James Clark Ross* officers and crew. Many other individuals contributed to the success of various components of the SeaWiFS Field Team activities within the AMT Program, including J. Brown, S. Maritorena, and C. Dempsey; their dedicated contributions are gratefully acknowledged. J. Brown is also thanked for his participation in the analysis of the optical data. The stewardship of the AMT Program was a high priority for J. Aiken; his diligence and commitment has been essential to the high quality and quantity of the field data collected. The AMT project and the resulting data archive would not have been possible without the unselfish contributions of many people at the Plymouth Marine Laboratory and the British Oceanographic Data Center. In particular, J. Aiken is acknowledged for initiating and coordinating the entire activity, M. Woodward is recognized for managing the nutrients analysis and making the data available, and A. Fairclough is thanked for the analysis and distribution of the XBT and CTD data sets. Finally, the authors wish to thank Drs. Carlos and Virginia Garcia for their useful comments.

# APPENDIX A

## Anomalous High Chlorophyll Event in the Fall of 1996

During the fall of 1996 (AMT-2), an anomalous chlorophyll concentration event occurred between 20°S and 30°S along the AMT cruise track. Except for the AMT-2 cruise, during which chlorophyll concentrations reached values above 0.2 $\mathrm{mg\,m^{-3}}$, chlorophyll concentrations at that latitude band were always below 0.1 $\mathrm{mg\,m^{-3}}$. This is shown in Figure A-1, which compares the meridional variability of near surface chlorophyll during AMT-2 with the corresponding variability during AMT-4. Both

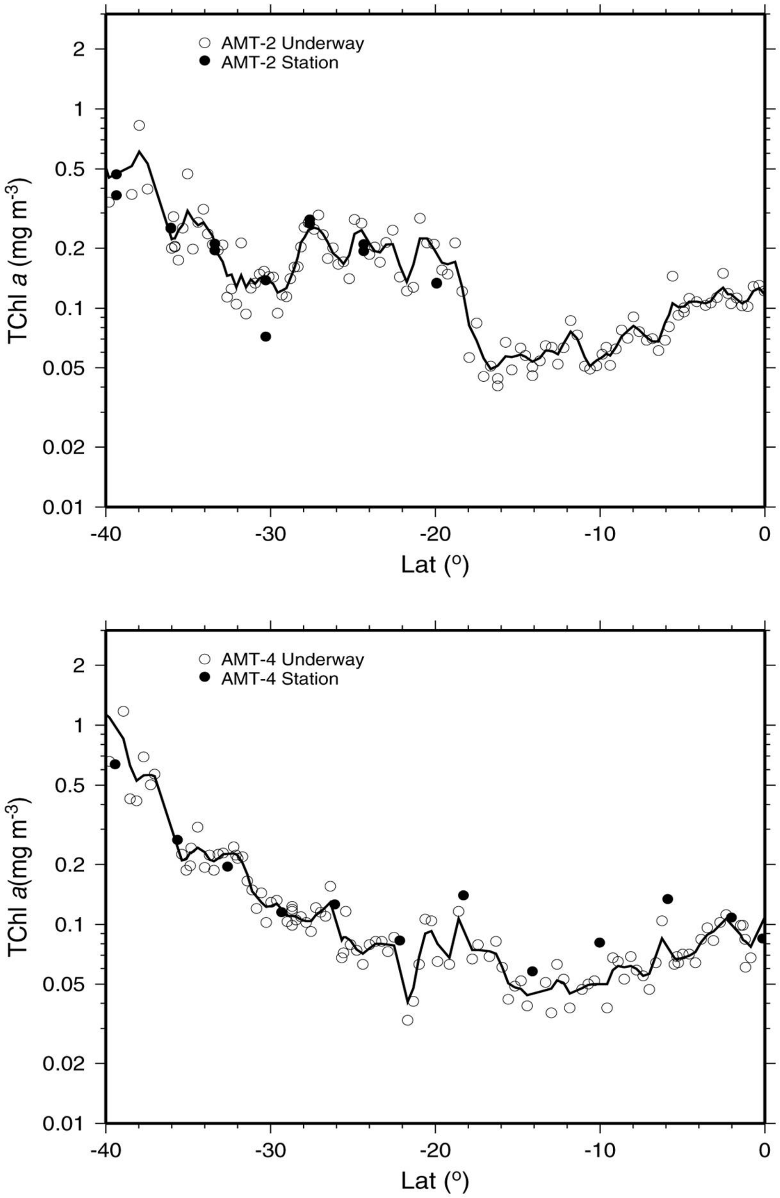

**Figure A-1.** Surface chlorophyll concentration as a function of latitude. The top plot shows data from AMT-2, while the bottom plot shows data from AMT-4. The blank circles correspond to underway observations and the filled circles correspond to station data. The lines are low-pass-filtered renditions of the data.

underway observations (blank circles) and near surface station observations (filled circles) show the striking difference between the two transects between 20$^o$S and 30$^o$S.

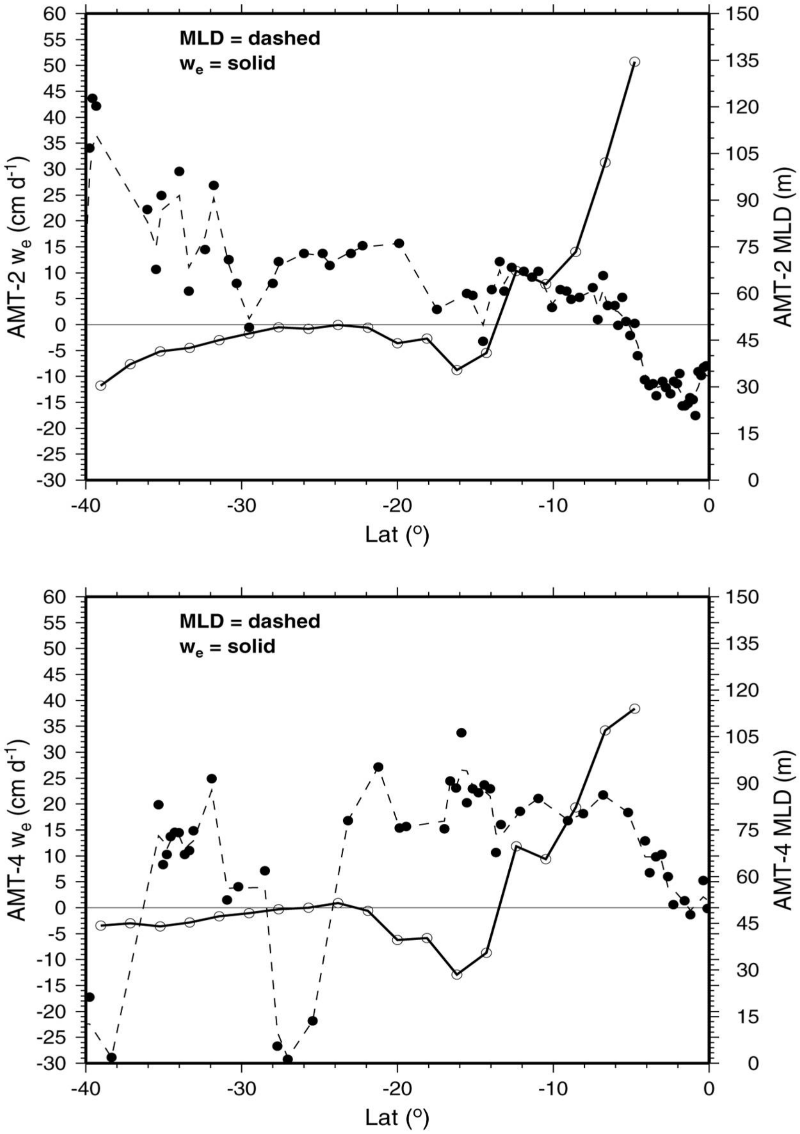

**Figure A-2.** Meridional variability of along-track (AMT-2 top, AMT-4 bottom) Ekman upwelling/downwelling ($w_e$) and mixed layer depth (MLD).

The meridional variability of the local physical forcing, e.g., the Ekman vertical velocity ($w_e$) and MLD, is shown in Figure A-2 for both AMT-2 and AMT-4 cruises. Between 20$^o$S and 30$^o$S, local physical forcing for AMT-2 clearly shows an increase in MLD from 50m outside this latitude range, to near 75m within that range. This 25m increase in MLD occurred during neutral Ekman forcing ($w_e$=0). The spatial coherence between the increased MLD and the elevated chlorophyll concentration seems to indicate that local mixing was the primary mechanism for the anomalous event.

An anomalous elevated chlorophyll event also occurred during AMT-4 (Figure A-1), but with chlorophyll concentrations (>0.1 mg m$^{-3}$) not as high as those recorded during AMT-2. This event occurred between 14°S and 22°S and coincided with deep local mixing (MLD of 75 to 90m), but concurrent with the strongest Ekman downwelling along the transect (Figure A-2). The interplay of deep mixing with strong downwelling seems to be the cause for the attenuated high chlorophyll event during AMT-4. Unfortunately, there are no concurrent satellite ocean color images to further analyze the extent and duration of these events. An analysis of SeaWiFS data (September 1997−August 2003), revealed that there were no similar events occurring during the 6 years of available ocean color data. This finding is an indication that the event that occurred in the fall of 1996 is somewhat rare.

## References

Aiken, J., and A.J. Bale, An introduction to the Atlantic Meridional Transect (AMT) programme, *Progress in Oceanography*, *45* (3-4), 251-256, 2000.

Aiken, J., D.G. Cummings, S.W. Gibb, N.W. Rees, R.S. Woodd-Walker, E.M.S. Woodward, J. Woolfenden, S.B. Hooker, J.-F. Berthon, C.D. Dempsey, D.J. Suggett, P. Wood, C. Donlon, N. Gonzalez-Benitez, I. Huskin, M. Quevedo, R. Barciela-Fernandez, C. de Vargas, and C. McKee, AMT-5 Cruise Report, NASA Tech. Memo. 1998-206892, Vol. 2, pp. 113 pp., NASA Goddard Sapce Flight Center, Greenbelt, Maryland, 1998.

Aiken, J., N. Rees, S. Hooker, P. Holligan, A. Bale, D. Robins, G. Moore, R. Harris, and D. Pilgrim, The Atlantic Meridional Transect: overview and synthesis of data, *Progress in Oceanography*, *45* (3-4), 257-312, 2000.

Bingham, F.M., Formation and Spreading of Subtropical Mode Water in the North Pacific, *Journal of Geophysical Research-Oceans*, *97* (C7), 11177-11189, 1992.

Carter Ohlmann, J., D.A. Siegel, and C. Gautier, Ocean mixed layer radiant heating and solar penetration: a global analysis, *Journal of Climate*, *vol.9, no.10*, 2265-2280, 1996.

Claustre, H., S.B. Hooker, L. Van Heukelem, J.-F. Berthon, R. Barlow, J. Ras, H. Sessions, C. Targa, C. Thomas, D. van der Linde, and J.-C. Marty, An intercomparison of HPLC phytoplankton pigment methods using in situ samples: Application to remote sensing and database activities, *Marine Chemistry*, (accepted), 2003.

Conkright, M., S. Levitus, T. O'Brien, T. Boyer, J. Antonov, and C. Stephens, World Ocean Atlas 1998 CD-ROM Data Set Documentation, *NODC Internal Report, Silver Spring, MD*, *Tech. Rep. 15*, 16 pp., 1998.

Craig, S.G., K.J. Holmen, G.B. Bonan, and P.J. Rasch, Atmospheric CO2 simulated by the National Center for Atmospheric Research Community Climate Model - 1. Mean fields and seasonal cycles, *Journal of Geophysical Research-Atmospheres*, *103* (D11), 13213-13235, 1998.

Evans, D.L., and S.R. Signorini, Vertical structure of the Brazil Current, *Nature*, *315*, 48-50, 1985.

Evans, D.L., S.R. Signorini, and L.B. Miranda, A Note on the Transport of the Brazil Current, *Journal of Physical Oceanography*, *13* (9), 1732-1738, 1983.

Gildor, H., A.H. Sobel, M.A. Cane, and R.N. Sambrotto, A role for ocean biota in tropical intraseasonal atmospheric variability (vol 30, art no 1460, 2003), *Geophysical Research Letters*, *30* (12), 2003.

Gordon, A.L., Oceanography - The brawniest retroflection, *Nature*, *421* (6926), 904-905, 2003.

Gordon, A.L., R.F. Weiss, W.M. Smethie, and M.J. Warner, Thermocline and Intermediate Water Communication between the South-Atlantic and Indian Oceans, *Journal of Geophysical Research-Oceans*, *97* (C5), 7223-7240, 1992.

Gruber, N., and J.L. Sarmiento, Global patterns of marine nitrogen fixation and denitrification, *Global Biogeochem. Cycles*, *11*, 235-366, 1997.

Hautala, S.L., and D.H. Roemmich, Subtropical mode water in the Northeast Pacific Basin, *Journal of Geophysical Research-Oceans*, *103* (C6), 13055-13066, 1998.

Hooker, S.B., and J. Aiken, Calibration evaluation and radiometric testing of field radiometers with the SeaWiFS Quality Monitor (SQM), *Journal of Atmospheric and Oceanic Technology*, *15*, 995-1007, 1998.

Hooker, S.B., H. Claustre, J. Ras, L. Van Heukelem, J.-F. Berthon, C. Targa, D. van der Linde, R. Barlow, and H. Sessions, The First SeaWiFS HPLC Analysis Round-Robin Experiment (SeaHARRE-1), NASA Tech. Memo. 2000-206892, Vol. 14, pp. 42 pp., Greenbelt, Maryland, 2000a.

Hooker, S.B., and G. Lazin, The SeaBOARR Field Campaign, NASA Tech. Memo. 2000-206892, Vol. 8, pp. 46 pp., Greenbelt, Maryland, 2000.

Hooker, S.B., and S. Maritorena, An evaluation of oceanographic radiometers and deployment methodologies, *Journal of Atmospheric and Oceanic Technology*, *17*, 811-830, 2000.

Hooker, S.B., S. McLean, J. Sherman, M. Small, G. Lazin, G. Zibordi, and J.W. Brown, The Seventh SeaWiFS Intercalibration Round-Robin Experiment (SIRREX-7), March 1999, NASA Tech. Memo. 2002-206892, pp. 69 pp., Greenbelt, Maryland, 2002.

Hooker, S.B., N.W. Rees, and J. Aiken, An objective methodology for identifying oceanic provinces, *Progress in Oceanography*, *45* (3-4), 313-338, 2000b.

Hooker, S.B., G. Zibordi, J.-F. Berthon, and J.W. Brown, Above-water radiometry in shallow, coastal waters, *Appl. Optics*, (submitted), 2003.

Hooker, S.B., G. Zibordi, J.-F. Berthon, D. D'Alimonte, S. Maritorena, S. McLean, and J. Sildam, Results of the Second SeaWiFS Data Analysis Round Robin, March 2000 (DARR-00), NASA Tech. Memo. 2001-206892, Vol. 15, pp. 71pp., Greenbelt, Maryland, 2001.

Johnson, B.C., P.-S. Shaw, S.B. Hooker, and D. Lynch, Radiometric and engineering performance of the SeaWiFS Quality Monitor (SQM): A portable light source for field radiometers, *J. Atmos. Oceanic Technol.*, *15*, 1008-1022, 1998.

Lee, K., R. Wanninkhof, T. Takahashi, S.C. Doney, and R.A. Feely, Low interannual variability in recent oceanic uptake of atmospheric carbon dioxide, *Nature*, *396* (6707), 155-159, 1998.

Lefevre, N., and G.F. Moore, Distribution of the CO2 partial pressure along an Atlantic Meridional transect, *Progress in Oceanography*, *45* (3-4), 401-413, 2000.

Lefevre, N., and A. Taylor, Estimating pCO(2) from sea surface temperatures in the Atlantic gyres, *Deep-Sea Research Part I-Oceanographic Research Papers*, *49* (3), 539-554, 2002.

Lewis, M.R., M.E. Carr, G.C. Feldman, W. Esaias, and C. McClain, Influence of Penetrating Solar-Radiation on the Heat-Budget of the Equatorial Pacific-Ocean, *Nature*, *347* (6293), 543-545, 1990.

Lewis, M.R., J.J. Cullen, and T. Platt, Phytoplankton and Thermal Structure in the Upper Ocean - Consequences of Nonuniformity in Chlorophyll Profile, *Journal of Geophysical Research-Oceans and Atmospheres*, *88* (NC4), 2565-2570, 1983.

Longhurst, A., S. Sathyendranath, T. Platt, and C. Caverhill, An estimate of global primary production in the ocean from satellite radiometer data, *Journal of Plankton Research*, *17*, 1245-1271, 1995.

Marañón, E., P.M. Holligan, M. Varela, B. Mouriño, and A.J. Bale, Basin-scale variability of phytoplankton biomass, production and growth in the Atlantic Ocean, *Deep-Sea Res. I*, *47*, 825-857, 2000.

McClain, C.R., S.R. Signorini, and J.R. Christian, Subtropical gyre variability observed by ocean color, *Deep-Sea Res. Part II*, in press, 2003.

McGillicuddy, D.J., A.R. Robinson, D.A. Siegel, H.W. Jannasch, R. Johnson, T.D. Dickey, J. McNeil, A.F. Michaels, and A.H. Knap, Influence of mesoscale eddies on new production in the Sargasso Sea, *Nature*, *394*, 263-265, 1998.

Mueller, J.L., SeaWiFS Algorithm for the Diffuse Attenuation Coefficient, *K*(490), Using Water-Leaving Radiances at 490 and 555 nm, in *SeaWiFS Postlaunch Technical Report Series, SeaWiFS Postlaunch Calibration and Validation Analyses, Part 3*, edited by S.B. Hooker, and E. Firestone, pp. 24-27, NASA Goddard Space Flight Center, Greenbelt, 2000.

Murtugudde, R., J. Beauchamp, C.R. McClain, M. Lewis, and A.J. Busalacchi, Effects of penetrative radiation on the upper tropical ocean circulation, *Journal of Climate*, *15* (5), 470-486, 2002.

Nelson, N.B., N.R. Bates, D.A. Siegel, and A.F. Michaels, Spatial variability of the CO2 sink in the Sargasso Sea, *Deep-Sea Research Part Ii-Topical Studies in Oceanography*, *48* (8-9), 1801-1821, 2001.

O'Reilly, J.E., S. Maritorena, M.C. O'Brien, D.A. Siegel, D. Toole, D. Menzies, R.C. Smith, J.L. Mueller, B.G. Mitchell, M. Kahru, F. Chavez, P. Strutton, G.F. Cota, S.B. Hooker, C.R. McClain, K.L. Carder, F. Müller-Karger, L. Harding, A. Magnuson, D. Phinney, G.F. Moore, J. Aiken, K.R. Arrigo, R.M. Letelier, and M. Culver, Volume 11, SeaWiFS Postlaunch Calibration and Validation Analyses, Part 3, SeaWiFS Postlaunch Technical Report Series, S. B. Hooker and R. R. Firestone, Editors, NASA/TM-2000-206892, Vol. 11, pp. 49, NASA, Greenbelt, Maryland, 2000.

Oschlies, A., Can eddies make ocean deserts bloom?, *Global Biogeochem. Cycles*, *16* (4), 1106, doi:10.1029/2001GB001830, 2002a.

Oschlies, A., Nutrient supply to the surface waters of the North Atlantic: A model study, *Journal of Geophysical Research-Oceans*, *107* (C5), art. no.-3046, 2002b.

Oschlies, A., and V. Garçon, Eddy-induced enhancement of primary production in a model of the north Atlantic Ocean, *Nature*, *394* (6690), 266-269, 1998.

Peterson, R.G., and L. Stramma, Upper-Level Circulation in the South-Atlantic Ocean, *Progress in Oceanography*, *26* (1), 1-73, 1991.

Planas, D., S. Agusti, C.M. Duarte, T.C. Granata, and M. Merino, Nitrate uptake and diffusive nitrate supply in the Central Atlantic, *Limnology and Oceanography*, *44* (1), 116-126, 1999.

Reid, J.L., On the Total Geostrophic Circulation of the South-Atlantic Ocean - Flow Patterns, Tracers, and Transports, *Progress in Oceanography*, *23* (3), 149-244, 1989.

Reynolds, R.W., and T.M. Smith, Improved Global Sea-Surface Temperature Analyses Using Optimum Interpolation, *Journal of Climate*, *7* (6), 929-948, 1994.

Robins, D.B., A.J. Bale, G.F. Moore, N.W. Rees, S.B. Hooker, C.P. Gallienne, A.G. Westbrook, E. Maranon, W.H. Spooner, and S.R. Laney, AMT-1 Cruise Report and Preliminary Results, NASA Tech. Memo. 104566. Vol. 35, pp. 87 pp., Greenbelt, Maryland, 1996.

Siegel, D.A., J.C. Ohlmann, L. Washburn, R.R. Bidigare, C.T. Nosse, E. Fields, and Z. Yimei, Solar radiation, phytoplankton pigments and the radiant heating of the equatorial Pacific warm pool, *Journal of Geophysical Research*, *vol.100, no.C3*, 4885-4891, 1995.

Signorini, S.R., On the circulation and volume transport of the Brazil Current between the Cape of Sao Tome and Guanabara Bay, *Deep-Sea Res. I*, *25* (5), 481-590, 1978.

Signorini, S.R., and C.R. McClain, Sensitivity of Global Sea-Air CO2 Flux to Gas Transfer Algorithms, Climatological Wind Speeds, and Variability of Sea Surface Temperature and Salinity, pp. 25, NASA Goddard Space Flight Center, Greenbelt, 2002.

Sprintall, J., and M.F. Cronin, Upper Ocean Vertical Structure, in *Encyclopedia of Ocean Sciences*, edited by J.H. Steele, K.K. Turekian, and S.A. Thorpe, pp. 3118-3126, Academic Press, 2001.

Stramma, L., The Brazil Current Transport South of 23-Degrees-S, *Deep-Sea Research Part a-Oceanographic Research Papers*, *36* (4), 639-646, 1989.

Stramma, L., Y. Ikeda, and R.G. Peterson, Geostrophic Transport in the Brazil Current Region North of 20-Degrees-S, *Deep-Sea Research Part a-Oceanographic Research Papers*, *37* (12), 1875-1886, 1990.

Suga, T., Y. Takei, and K. Hanawa, Thermostad distribution in the North Pacific subtropical gyre: The General mode water and the subtropical mode water, *Journal of Physical Oceanography*, *27* (1), 140-152, 1997.

Takahashi, T., R.A. Feely, R.F. Weiss, R.H. Wanninkhof, D.W. Chipman, S.C. Sutherland, and T.T. Takahashi, Global air-sea flux of $CO_2$: An estimate based on measurements of sea-air $pCO_2$ difference, *Proceedings of the National Academy of Sciences of the United States of America*, *94* (16), 8292-8299, 1997.

Wanninkhof, R., Relationship between Wind-Speed and Gas-Exchange over the Ocean, *Journal of Geophysical Research-Oceans*, *97* (C5), 7373-7382, 1992.

Weiss, R.F., and B.A. Price, Nitrous oxide solubility in water and seawater, *Mar. Chem.*, *8*, 347-359, 1980.

Williams, R.G., and M.J. Follows, The Ekman transfer of nutrients and maintenance of new production over the North Atlantic, *Deep-Sea Research Part I-Oceanographic Research Papers*, *45* (2-3), 461-489, 1998.

Witter, D.L., and A.L. Gordon, Interannual variability of South Atlantic circulation from 4 years of TOPEX/POSEIDON satellite altimeter observations, *Journal of Geophysical Research-Oceans*, *104* (C9), 20927-20948, 1999.

# REPORT DOCUMENTATION PAGE

*Form Approved*
*OMB No. 0704-0188*

**1. AGENCY USE ONLY *(Leave blank)***

**2. REPORT DATE**
December 2003

**3. REPORT TYPE AND DATES COVERED**
Technical Memorandum

**4. TITLE AND SUBTITLE**
*Bio-Optical and Geochemical Properties of the South Atlantic Subtropical Gyre*

**5. FUNDING NUMBERS**
Code 970

**6. AUTHOR**
*S. Signorini, S. Hooker, C. McClain*

**7. PERFORMING ORGANIZATION NAME(S) AND ADDRESS(ES)**
*NASA/GSFC*
*Code 970.2*
*Greenbelt MD 20771*

**8. PERFORMING ORGANIZATION REPORT NUMBER**
2004-00663-0

**9. SPONSORING/MONITORING AGENCY NAME(S) AND ADDRESS(ES)**
National Aeronautics and Space Administration
Washington, D.C. 20546–0001

**10. SPONSORING/MONITORING AGENCY REPORT NUMBER**
TM-2003-212253

**11. SUPPLEMENTARY NOTES**

**12a. DISTRIBUTION/AVAILABILITY STATEMENT**
Unclassified–Unlimited
Subject Category 48
Report is available from the Center for AeroSpace Information (CASI),
7121 Standard Drive, Hanover, MD 21076–1320; (301)621-0390

**12b. DISTRIBUTION CODE**

**13. ABSTRACT***S (Maximum 200 words)*

*An investigation of the bio-optical properties of the South Atlantic subtropical gyre (SASG) was conducted using data primarily from the UK Atlantic Meridional Transect (AMT) program and SeaWiFS. The AMT cruises extend from the UK to the Falklands Islands (sailing on the RRS James Clark Ross) with the purpose of improving our knowledge of surface layer hydrography, biogeochemical processes, ecosystem dynamics and food webs across basin scales in the Atlantic Ocean [Aiken et al., 2000]. Two objectives of the AMT program relevant to this study are the characterization of biogeochemical provinces and the analysis of optical and pigment parameters in connection with remote sensing ocean color data.*

*The primary focus of this NASA Technical Memorandum is on the variability of the vertical distribution of phytoplankton pigments and associated absorption properties across the SASG, and their relevance to remote sensing algorithms. Therefore, a subset of the AMT data within the SASG from all available cruises was used in the analyses. One of the challenges addressed here is the determination of the SASG geographic boundaries. One of the major problems is to reconcile the properties of biogeochemical provinces [Longhurst et al., 1995] with the boundaries of physical provinces [Hooker et al., 2000b]. We use water mass analysis, dynamics of ocean currents, and meridional gradients of bio-optical properties, to identify the SASG boundaries.*

*The variability of the sea-air pCO2 difference (DpCO2) and corresponding CO2 flux are also analyzed in this TM. Atmospheric and oceanic pCO2 were measured continuously [Lefevre and Moore, 2000] along an AMT transect (50oN-50oS) in September-October 1995 and 1996 (UK to the Falklands Islands) and in April-May 1996 (Falklands Islands to the UK). Based on data from these three AMT cruises, and data from two other cruises (M/V Prince of Seas sailing from UK to Jamaica and RMS St. Helena sailing from UK to South Africa), Lefevre and Taylor [2002] developed a pCO2 algorithm for the North Atlantic and South Atlantic gyres. We used the pCO2 algorithm to estimate the seasonal variability of DpCO2 and sea-air CO2 flux in the SASG.*

**14. SUBJECT TERMS**

**15. NUMBER OF PAGES**
48

**16. PRICE CODE**

| | | | |
|---|---|---|---|
| **17. SECURITY CLASSIFICATION OF REPORT** | **18. SECURITY CLASSIFICATION OF THIS PAGE** | **19. SECURITY CLASSIFICATION OF ABSTRACT** | **20. LIMITATION OF ABSTRACT** |
| Unclassified | Unclassified | Unclassified | Unlimited |

D